Supporting Information

Ligand-substituted inorganic-organic hybrid materials for efficient urea-assisted electrocatalytic water splitting

Lingshen Meng[†1], Zeyi Zhang[†1], Carlos A. Triana[*1], Aaron A. Schultz[1], Hang Chen[1], Dan Zhang[2], and Greta R. Patzke[*1]

[1] Department of Chemistry, University of Zurich, Winterthurerstrasse 190, CH-8057 Zurich, Switzerland

[2] China Frontiers Science Center for Deep Ocean Multisphases and Earth System/Key Laboratory of Marine Chemistry Theory and Technology, Ministry of Education, Ocean University of China, 266100, Qingdao, P.R. China

[†] These authors contributed equally: Lingshen Meng and Zeyi Zhang

* Email of corresponding author: carlos.triana@chem.uzh.ch, greta.patzke@chem.uzh.ch

Contents

S1. Experimental Section

S1.1. Materials

Raw chemicals including nickel chloride ($NiCl_2$), pyrimidine (pm), pyrazine (pz), 4,4'-bipyridine (bpy), deuterium oxide (D_2O), and sodium formate (HCOONa) were purchased from Thermo Fisher Scientific. Potassium hydroxide (KOH), N,N-dimethylformamide (DMF), acetone, urea, methanol, benzyl alcohol and Nafion (5 wt%) solution were obtained from Sigma-Aldrich, ethanol was obtained from VWR international S.A.S. All chemicals of analytical grade and used without further purification.

Hydrochloric acid solution (HCl, 37 wt%) and nitric acid solution (HNO_3, 65 wt%) were purchased from Superlco.

The anion exchange membrane (Nafion 117, USA) was purchased from The Chemours Company, LLC, while carbon paper (MGL190, USA) was obtained from AvCarb Material Solutions.

S1.2. Carbon paper and carbon black cleaning

The cleaning of carbon paper (CP) was carried out in two steps. Initially, a small piece of CP measuring 1×2 cm^2 was ultrasonically cleaned in acetone for approximately 15 min to remove any organic species on the CP surface, followed by rinsing twice with ethanol. Subsequently, the CP was further ultrasonically cleaned in 1 M HCl for 15 min to eliminate some oxides present on the CP surface and then rinsed again with ethanol. After washing, the CP was dried in an oven at 60 ℃ for 30 min. The carbon black was also washed in ethanol and HCl solutions under the same conditions.

S1.3. Materials Synthesis

NiClOH-L: The hybrid materials were prepared using methods similar to those previously reported.[1] Taking NiClOH-Pm as an example, $NiCl_2$ (0.216 g, 1.67 mmol) was dissolved in 20 mL DMF (N,N-dimethylformamide), and then 1 mL of H_2O was added to a vial. Pyrimidine (135 μL, 1.71 mmol) was subsequently added to the solution. The mixture was heated at 120 ℃ for 24 h, resulting in a green sample. This sample was washed three times with water and ethanol. After isolation by centrifugation and air drying, NiClOH-Pm was obtained.

NiClOH-Pm_xPz_{1-x}: The ligand-substituted hybrid materials with varying ratios were synthesized via hydrothermal reactions. Specifically, a mixture of NiClOH-Pm and different proportions (the initial ratio ranged from 10% to 90 at%) of pyrazine were added in a vial with 20 mL of DMF and 1 mL of H_2O as the solvent. The mixture was then heated at 120 ℃ for 24 h, yielding light green to light blue samples. These samples were subsequently washed three times with water and ethanol. Following isolation by centrifugation and air drying, a series of NiClOH-Pm_xPz_{1-x} hybrid compounds were obtained (Figure S1).

$Ni(OH)_2$: $Ni(OH)_2$ was synthesized via hydrothermal reaction. $Ni(NO_3)_2 \cdot 6H_2O$ (0.182 g, 1 mmol) was dissolved in 20 mL DMF in a vial. Then 1 mol L^{-1} KOH was added dropwise to adjust the pH to 8.0. The mixture was heated at 120 ℃ for 24 h. Finally, the sample was washed by water and ethanol three times and dried in air overnight.

S1.4. Electrocatalyst ink preparation

For the catalysts ink preparation, 4 mg of catalysts, 0.8 mg carbon black and 20 μL of 5 wt% Nafion solution was dispersed in 980 μL of 1:3 v/v of water/ethanol mixture and then ultrasonicated for about half an hour to form homogeneous ink-like dispersion. Then a total of 100 μL of the ink (containing 0.4 mg of catalysts) was dropped cast on a 1 cm^2 cleaned CP. Finally, the CP with catalyst ink was dried at room temperature.

For the working electrode applied for *in situ* Raman spectroscopy measurements, 10 mg of hybrid materials, and 20 μL of 5 wt% Nafion solution was dispersed in 980 μL of 1:3 v/v of water/ethanol mixture and then ultrasonicated for about half hour to form a homogeneous ink-like dispersion. For enhanced Raman spectra, a total of 200 μL of the ink (containing 0.5 mg of catalysts) was drop cast on a 2 × 2 cm^2 fluorine-doped tin oxide (FTO) glass. Finally, the FTO glass with catalyst ink was dried at room temperature.

S1.5. Electrochemical measurements

All electrochemical performance tests were conducted at room temperature utilizing a standard three-electrode system within a typical H-type cell. The electrochemical workstation employed for these measurements was the Metrohm Autolab PGSTAT302N. However, for cyclic voltammograms (CV) measurements relating to electrochemical double layer capacitance (EDLC), scans were carried out at various rates ranging from 10 to 50 $mV \cdot s^{-1}$ using the same electrochemical workstation. Pt wire served as counter electrode (CE) and Ag/AgCl electrode with saturated KCl filling solution acted as reference electrode (RE). The CP with as-prepared sample was used as the working electrode (WE). The potentials were converted to the reversible hydrogen electrode (RHE) scale in terms of the calibration equation as follows,

$$E\,(RHE) = E\,(Ag/AgCl) + 0.059 \times pH + 0.197$$

where pH = 14 in 1.0 M KOH and 0.5 M urea solution.

Linear scan voltammetry (LSV) was performed at a scan rate of 10 $mV \cdot s^{-1}$ in 1 M KOH and 0.5 M urea, and all data were modified without ohmic potential drop (iR) correction. Prior to the electrochemical experiment, the WE were first cycled several times in a potential window from 0.8 to 1.8 V (vs. RHE) at scan rate 100 $mV \cdot s^{-1}$ until a reproducible voltammogram was obtained.

The 24 h stability test of the as-synthesized hybrid materials for UOR was performed in 1 M KOH and 0.5 M urea at room temperature for 24 h at 10 mA cm^{-2}. Stability tests on different biomass oxidation reactions were performed in 1 M KOH and 0.5 M corresponding biomass mixed solution.

The selectivity of UOR versus with OER was calculated with O_2 evolution rate measured by gas chromatography (GC). The gases produced during electrolysis were analyzed online using a GC-3000 ET Fusion (Inficon Instruments) GC fitted with 10 m packed molecular-sieve columns. O_2 and N_2 were quantified by a thermal conductivity detector (TCD), while H_2 was measured with a flame ionization detector (FID). At three-minute intervals during galvanostatic UOR experiments, volatile products were swept from the headspace of cell into the 10 μL sampling loop of GC by an argon carrier flow (99.999%, Landt, Switzerland) of 10 mL min^{-1}, regulated by a mass-flow controller. Continuous argon flow through the electrolysis cell ensured efficient transfer of reaction products into the chromatograph for real-time quantification.

The Faradaic efficiency (FE) of the UOR was quantitatively calculated by analyzing the NMR spectra

of the samples before and after the reaction, and then calculated using the following formula.

$$FE = \frac{nF\Delta m}{It} \times 100\%$$

where n is the number of the transferred electrons; F is Faraday constant (96485 C mol^{-1}); Δm is the consumption of moles of urea; I is the current value; t is the reaction time.

S1.6. Characterization methods

Powder X-ray diffraction (XRD) measurements were performed on a STOE STADI P diffractometer (transmission mode, Ge monochromator) with Cu K_α radiation ($K_{\alpha1}$ = 1.15417 Å) operated at 50 kV and 40 mA. The data were refined with the Rietica program using the Le Bail method.

Field-emission scanning electron microscopy (SEM) images and corresponding energy-dispersive X-ray spectroscopy (EDS) mapping of all samples were performed on a Zeiss SUPRA 50VP. Transmission electron microscope (TEM) images were obtained using an FEI Tecnai G2 Spirit instrument.

X-ray photoelectron spectroscopy (XPS) data were obtained from 0 to 1200 eV using an ESCALAB 250 spectrometer (Thermo Fisher Scientific) equipped with an Al K_α (1486.6 eV) monochromatic source. The pass energy was set at 25 eV for the survey spectra, and overall resolution is 0.5 eV. The sensitivity factors are 2.88, 2.74, and 20.76 for O, Cl, and Ni, respectively. The charging shift was corrected using C 1s photoemission line at a binding energy of 284.8 eV.

Fourier transform infrared (FT-IR) spectra of the samples were recorded on a Bruker Vertex 70 spectrometer equipped with a Platinum ATR accessory containing a diamond crystal in the wavenumber range of 400 - 4000 cm^{-1}.

Ex situ Raman spectra were recorded on an inVia Qontor with a 532 nm excitation laser operating at 0.5% intensity. *In situ* Raman spectra were also recorded on same equipment and laser, but the intensity was 5%. The laser power at the sample was ≤ 5 mW to prevent laser damage of samples. A grating of 1800 grooves/mm was used. The resolution was 5 cm^{-1}, with the wavenumber accuracy of 2 cm^{-1}.

^{1}H NMR spectra of the samples were recorded on a Bruker AV2-401 spectrometer (400 MHz 1H frequency), and the longitudinal relaxation times (T1) were determined using the inversion recovery method. 0.1 mg samples were dissolved in 50 μL HNO_3 and 450 μL D_2O, ultrasonically dispersed for several seconds to obtain a light green solution for measurements. ^{1}H NMR and ^{13}C NMR spectra of the electrolyte before and after 24 h of testing were also recorded on a BRUKER AV2-401 spectrometer (400 MHz 1H frequency), and the longitudinal relaxation times (T1) were determined using the inversion recovery method. 200 μL electrolyte, 125 μL D_2O and 200 μL 1 M HCOONa were added into the NMR tube and ultrasonically dispersed for several seconds to obtain transparent and colorless solutions for measurements.

Thermogravimetric analysis (TGA) was conducted using a Netzsch simultaneous thermal analyzer (STA 409 CD). Approximately 10 mg of powdered sample was placed in an alumina crucible, which was wrapped in aluminum oxide foil to ensure thermal stability and uniform heat distribution. All measurements were carried out under a N_2 atmosphere to prevent oxidation and other atmospheric interactions. To correct for buoyancy and gas flow effects, a blank scan (conducted without the sample) was subtracted from the sample measurements. After analysis, the sample was cooled under N_2 to maintain an inert environment throughout the process.

The specific surface area was determined with the Brunauer–Emmett–Teller (BET) method. N_2 adsorption and desorption isotherms were measured at 77 K on a KICT SPA-3000 Gas Adsorption Analyzer after around 200 mg sample was degassed at 423 K to 20 mTorr for 12 h. The specific surface areas were determined from nitrogen adsorption.

X-ray absorption near-edge structure (XANES), and extended X-ray absorption fine structure (EXAFS) experiments were performed at the Ni *K*-edge on carbon paper substrates loaded with samples of NiClOH-Pm, NiClOH-$Pm_{0.8}Pz_{0.2}$ and their corresponding samples after 24 h UOR and reference $Ni(OH)_2$ in florescence mode at the BM31 beamline at the European Synchrotron Radiation Facility (ESRF), Grenoble, France. The energy was scanned with a double Si[111] crystal monochromator. The $k^3\chi(k)$ spectra were extracted by data reduction, absorption edge energy calibration and background subtraction using ATHENA.[2] All spectra were reduced into the range Δk=3-12 $Å^{-1}$ and Fourier-Transform to FT$|k^3\chi(k)|$ into the real-space interval ΔR=0-6 Å. Interatomic distances, coordination numbers (N), and Debye-Waller factors (σ^2), were obtained by non-linear least-squares fitting of the FT$|k^3\chi(k)|$ spectra by ARTEMIS.[2] The amplitude and phase shift for single/multiple scattering paths was calculated using FEFF6.[3] All EXAFS spectra FT$|k^3\chi(k)|$ were fitted without phase correction.

The room-temperature electron paramagnetic resonance (EPR) spectra were determined using a Bruker Magnettech MS-5000 at X-band (9.4 GHz), and the value of g was calculated by the following formula:

$$g = \frac{h\nu}{\mu_B B}$$

Where h is Planck's constant, ν is the microwave frequency (Hz), μ_B is the Bohr magneton, and B is the resonance magnetic field (T).

S1.7. Post-catalyst collection

In order to collect post-catalyst powder for characterization, the ink formula was adjusted as follows. Specifically, 0.8 mg NiClOH-$Pm_{0.8}Pz_{0.2}$ was dispersed in 950 μL anhydrous ethanol and 50 μL, 5% Nafion solution was added. In order to prevent the characterization from interference with other substances, carbon black was not added to the anhydrous ethanol. After ultrasonic dispersion for 30 min, these inks were dropped on 1×2 cm^2 FTO every 50 μL, air-dried and used for 24 h, 10 mA cm^{-2} long-term test of current density. After 24 h, the powder on the FTO was carefully scraped off for subsequent testing (SEM, EDX, Raman, FT-IR and XRD). Besides, the post-catalyst on carbon paper was also used for SEM/EDX characterizations.

S1.8. Density functional theory calculations

Density functional theory (DFT) calculations were carried out using the Vienna Ab-initio Simulation Package (VASP). The crystal structures of the NiOOH-PmPz supercells as the corresponding intermediate of NiClOH-$Pm_{0.8}Pz_{0.2}$ used in this study consist of 24 NiClOH + 24 $C_4H_4N_2$ (pyrimidine) and 24 NiOOH + 24 $C_4H_4N_2$ (pyrazine), with dimensions of 21.14 Å × 23.24 Å × 9.58 Å. NiOOH-SL, and NiOOH-Pm were also calculated as reference sample, referring to the corresponding intermediates of $Ni(OH)_2$ and NiClOH-Pm, respectively. The models with oxygen-vacancy (Vo) were constructed by removing one lattice oxygen atom from the NiOOH layers. The projector augmented wave (PAW) method was used to describe the ionic cores.[4] The electron exchange-correlation was modeled by the Perdew-Burke-Ernzerhof (PBE) function within the generalized gradient approximation (GGA).[5] Hubbard-U (DFT+U) calculations were included

with an effective U–J value of 5.5 eV for Ni.[6, 7] A plane-wave basis set with a cutoff energy of 450 eV was used to describe the valence electrons.[8] Γ-point sampling was adopted for k-space integration due to the large surface unit cell size.

The UOR steps include to the following schemes (1-8)：

$$CO(NH_2)_2\ (aq) \rightarrow CO(NH_2)_2* \quad (1)$$

$$CO(NH_2)_2* + OH^- \rightarrow CO(NH_2NH)* + H_2O + e^- \quad (2)$$

$$CO(NH_2NH)* + OH^- \rightarrow CO(NH_2N)* + H_2O + e^- \quad (3)$$

$$CO(NH_2N)* + OH^- \rightarrow CO(NHN)* + H_2O + e^- \quad (4)$$

$$CO(NHN)* + OH^- \rightarrow CON_2* + H_2O + e^- \quad (5)$$

$$CON_2* \rightarrow CO* + N_2\ (g) \quad (6)$$

$$CO* + OH^- \rightarrow *CO\text{-}OH + e^- \quad (7)$$

$$*CO\text{-}OH + OH^- \rightarrow CO_2(g) + H_2O + e^- \quad (8)$$

where * represents the active site and $CO(NH_2)_2$*, $CO(NH_2NH)$*, $CO(NH_2N)$*, $CO(NHN)$*, CON_2*, CO*, *CO-OH, are intermediates during the UOR process. The Gibbs free energy G for each species was calculated as follows:

$$G = E + ZPE - TS \quad (9)$$

where G, E, ZPE and TS are the free energy, total energy from DFT calculations, zero point energy and entropic contributions (T was set to be 300K), respectively. ZPE and TS could be derived after frequency calculation. Besides, the adsorption energies (ΔE_{ads}) of intermediates were calculated according to:

$$\Delta E_{ad} = E_{ads+sur} - E_{ads} - E_{sur} \quad (10)$$

$E_{ads+sur}$, E_{ads}, E_{sur} are the energies of surface with adsorbate, single adsorbate, and surface, respectively.

S2. Supporting Figures (Figures S1 – S37)

S2.1 Synthesis and characterization of NiClOH-PmPz electrocatalysts (Figures S1 – S6)

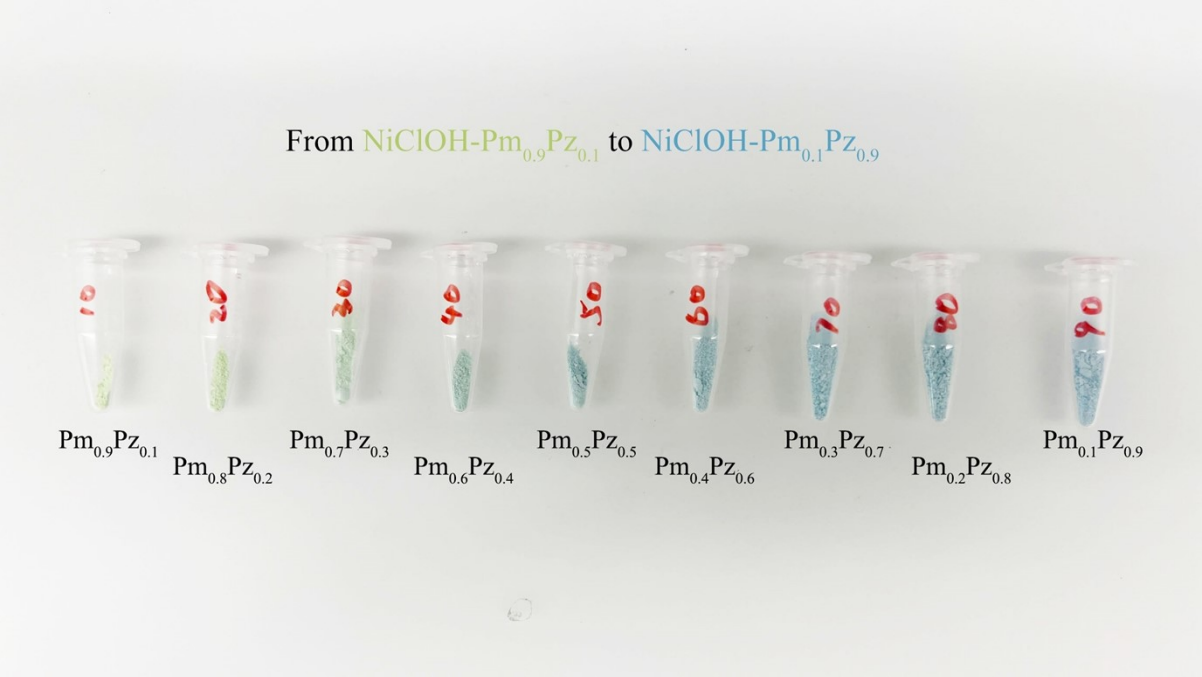

Figure S1. Powder samples of the NiClOH-Pm_xPz_{1-x} series (the numbers on the Eppendorf tubes refer to the percentage of pyrazine added during ligand replacement).

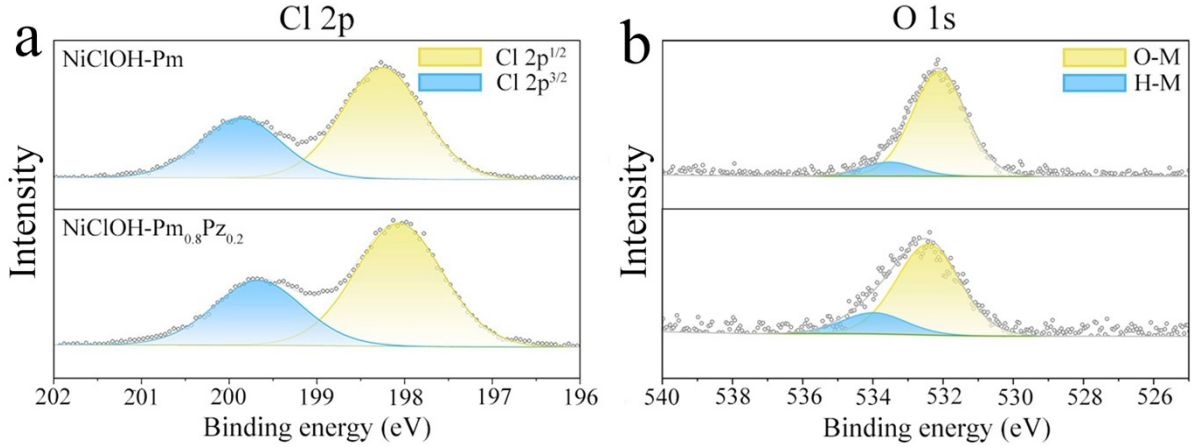

Figure S2. (a) High-resolution Cl 2p XPS and (b) O 1s XPS of NiClOH-Pm (top) and NiClOH-$Pm_{0.8}Pz_{0.2}$ (bottom).

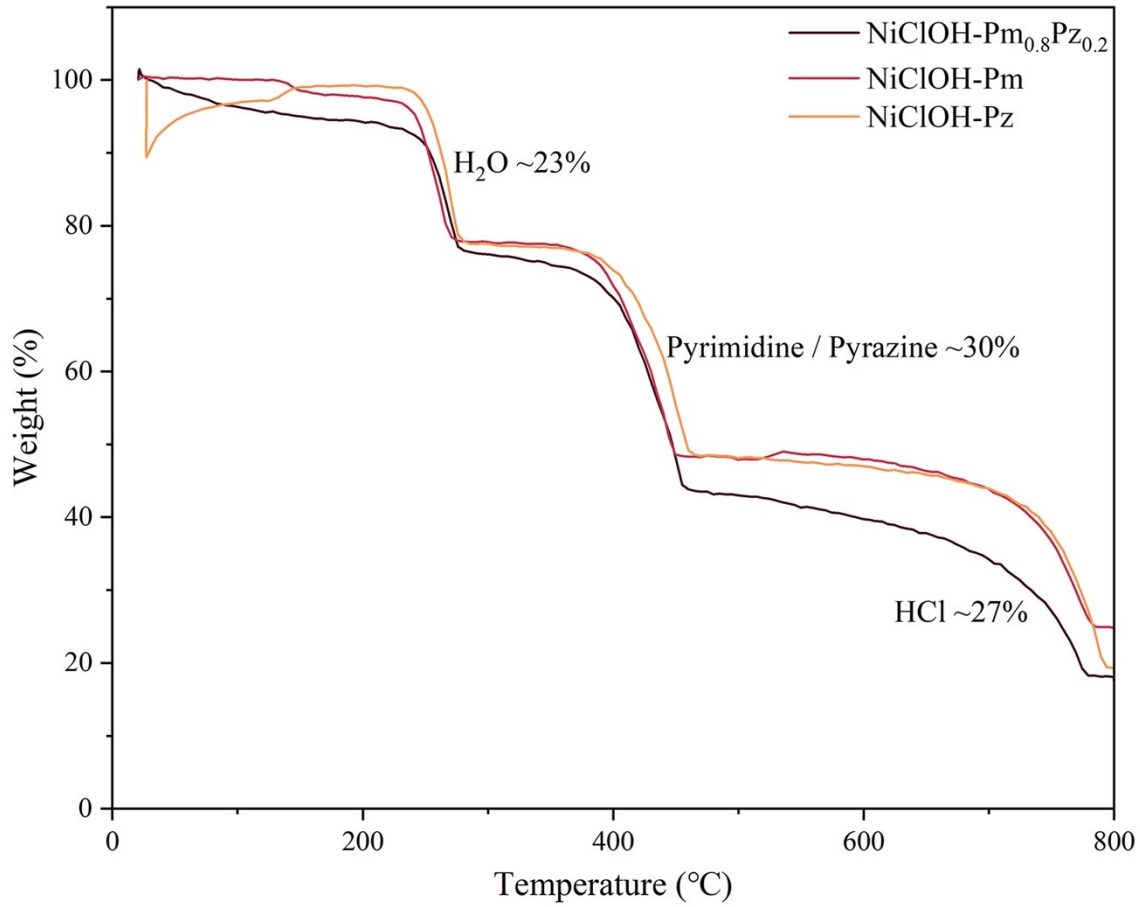

Figure S3. TGA profiles of NiClOH-$Pm_{0.8}Pz_{0.2}$, NiClOH-Pm and NiClOH-Pz.

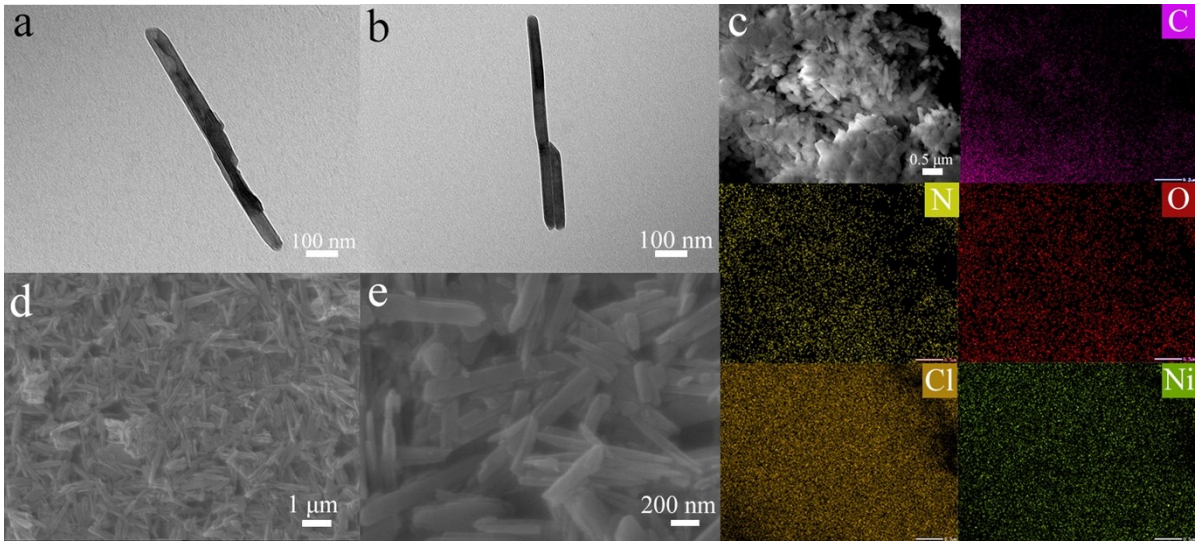

Figure S4. (a) TEM image of NiClOH-Pm; (b) TEM image of NiClOH-$Pm_{0.8}Pz_{0.2}$; (c) SEM and EDX mapping images of NiClOH- $Pm_{0.8}Pz_{0.2}$ on carbon paper; (d, e) SEM images of NiClOH-$Pm_{0.8}Pz_{0.2}$ on carbon paper.

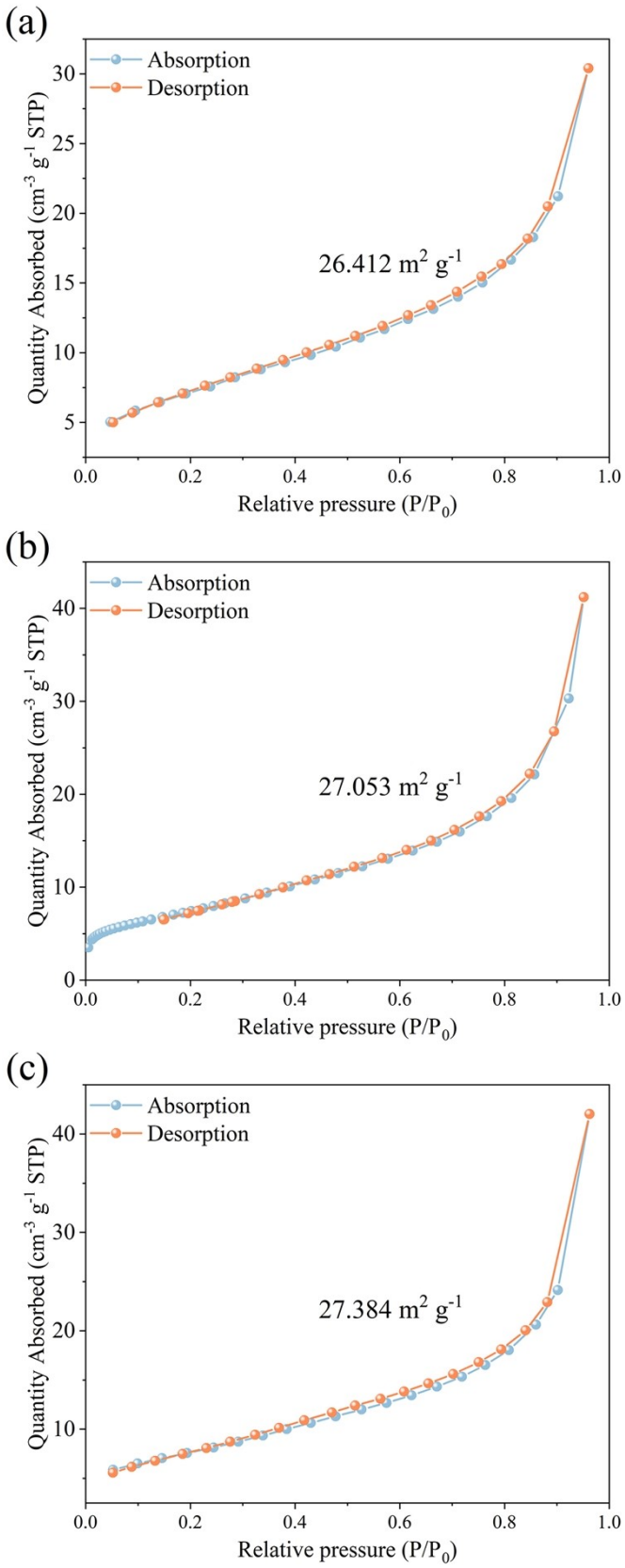

Figure S5. BET surface area analyses: N_2-adsorption-desorption isotherm plots of (a) NiClOH-Pm, (b) NiClOH-Pz, and (c) NiClOH-$Pm_{0.8}Pz_{0.2}$.

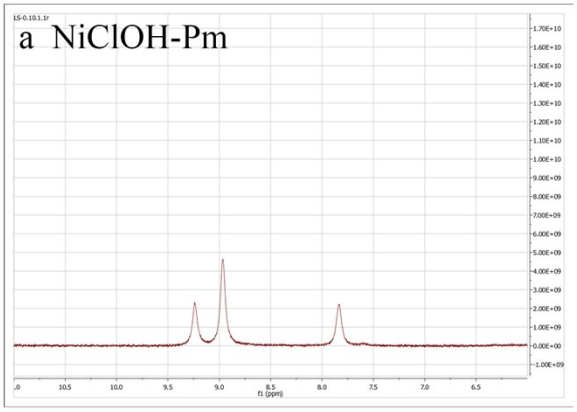
a NiClOH-Pm

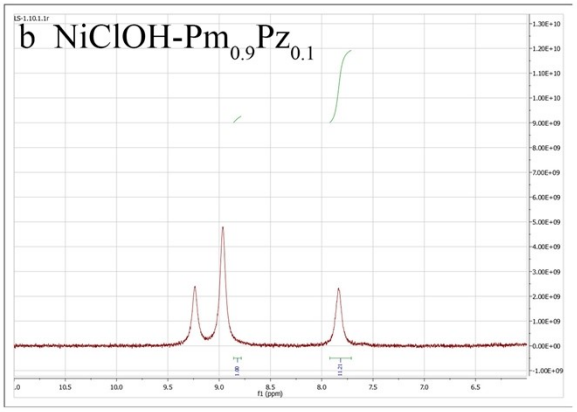
b NiClOH-Pm0.9Pz0.1

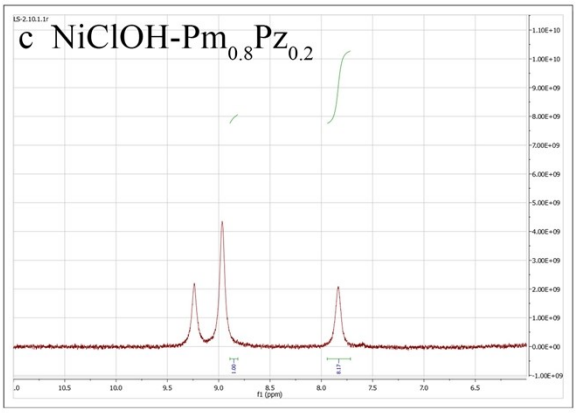
c NiClOH-Pm0.8Pz0.2

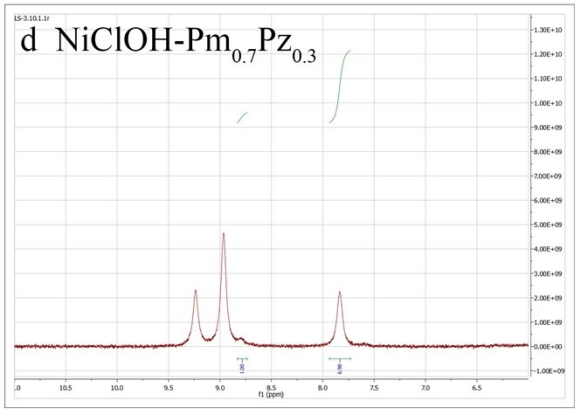
d NiClOH-Pm0.7Pz0.3

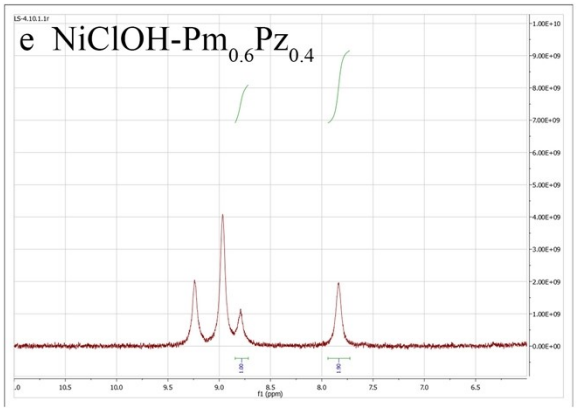
e NiClOH-Pm0.6Pz0.4

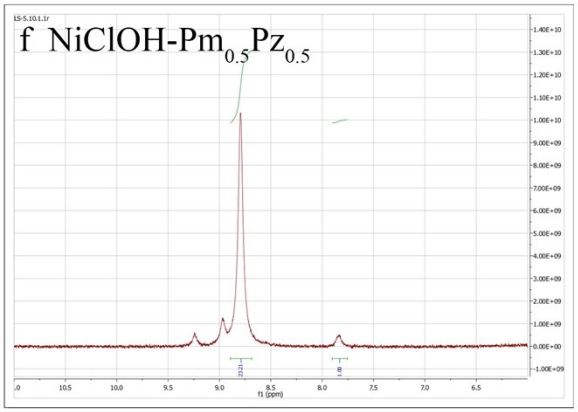
f NiClOH-Pm0.5Pz0.5

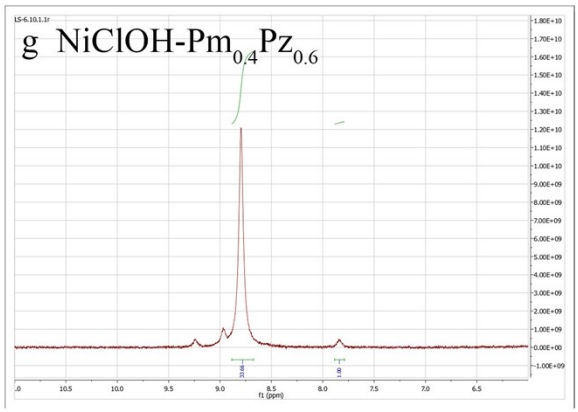
g NiClOH-Pm0.4Pz0.6

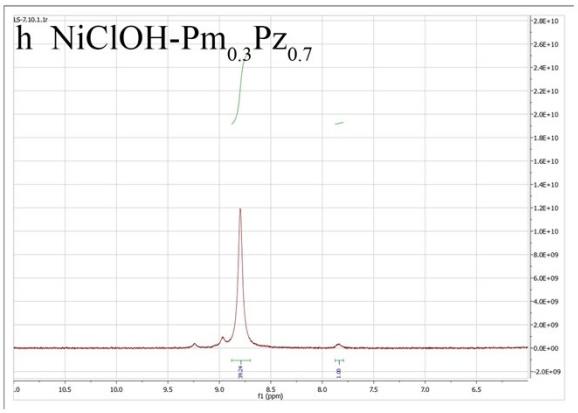
h NiClOH-Pm0.3Pz0.7

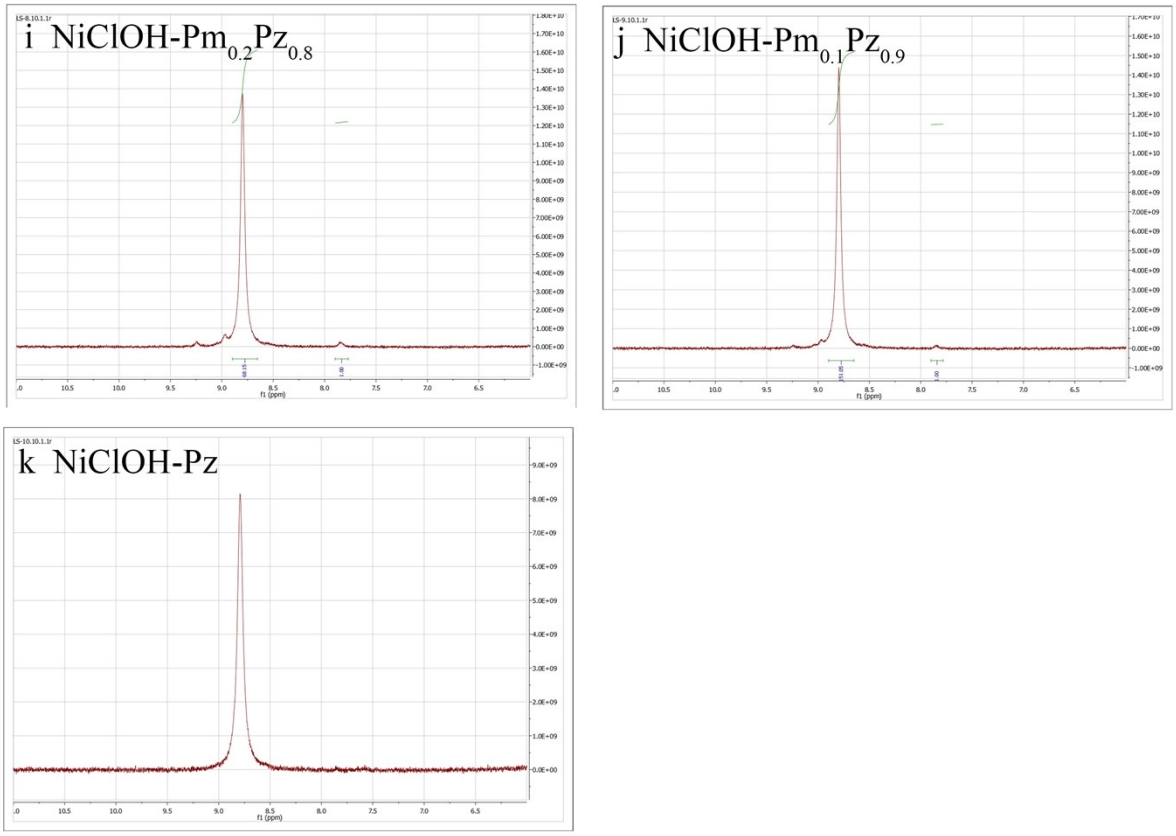

Figure S6. ^{1}H NMR spectra of NiClOH-Pm_xPz_{1-x} samples with different ligand ratios.

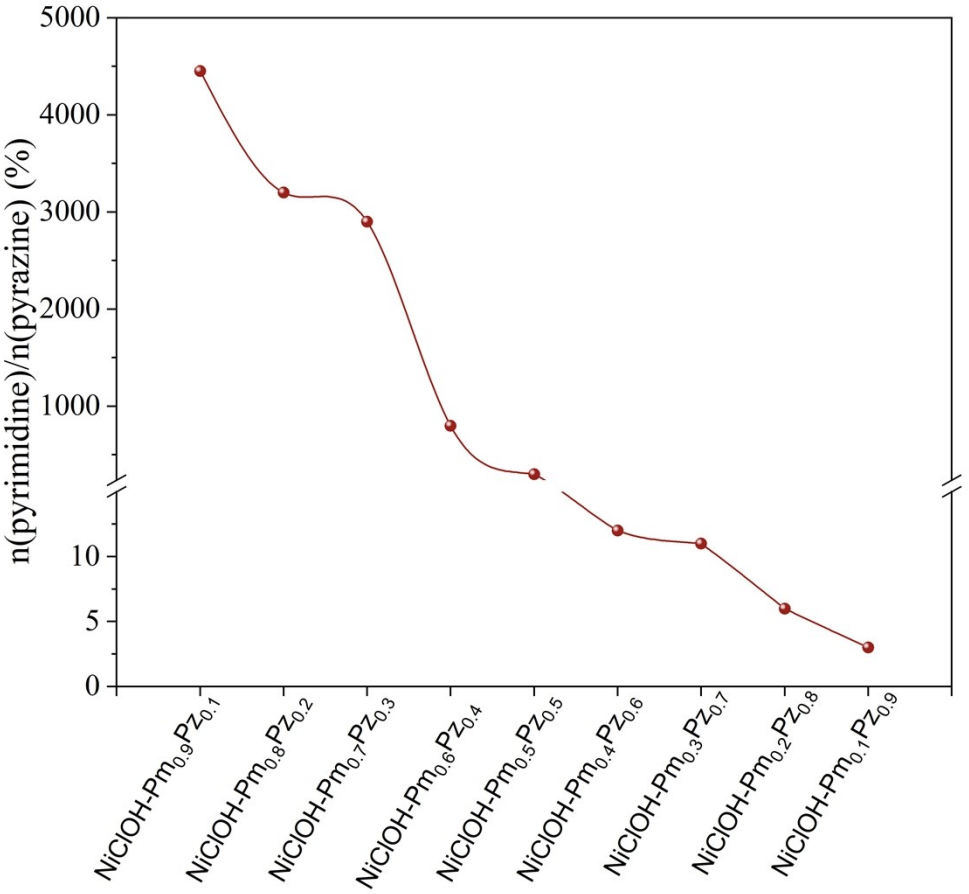

Figure S7. Ligand ratios of different NiClOH-Pm_xPz_{1-x} samples as obtained from the integration of the peak areas of the two groups of peaks of the ^{1}H NMR spectra shown in Figure S6.

S2.2 Inorganic-organic hybrids for urea electrochemical oxidation (Figure S7 – S21)

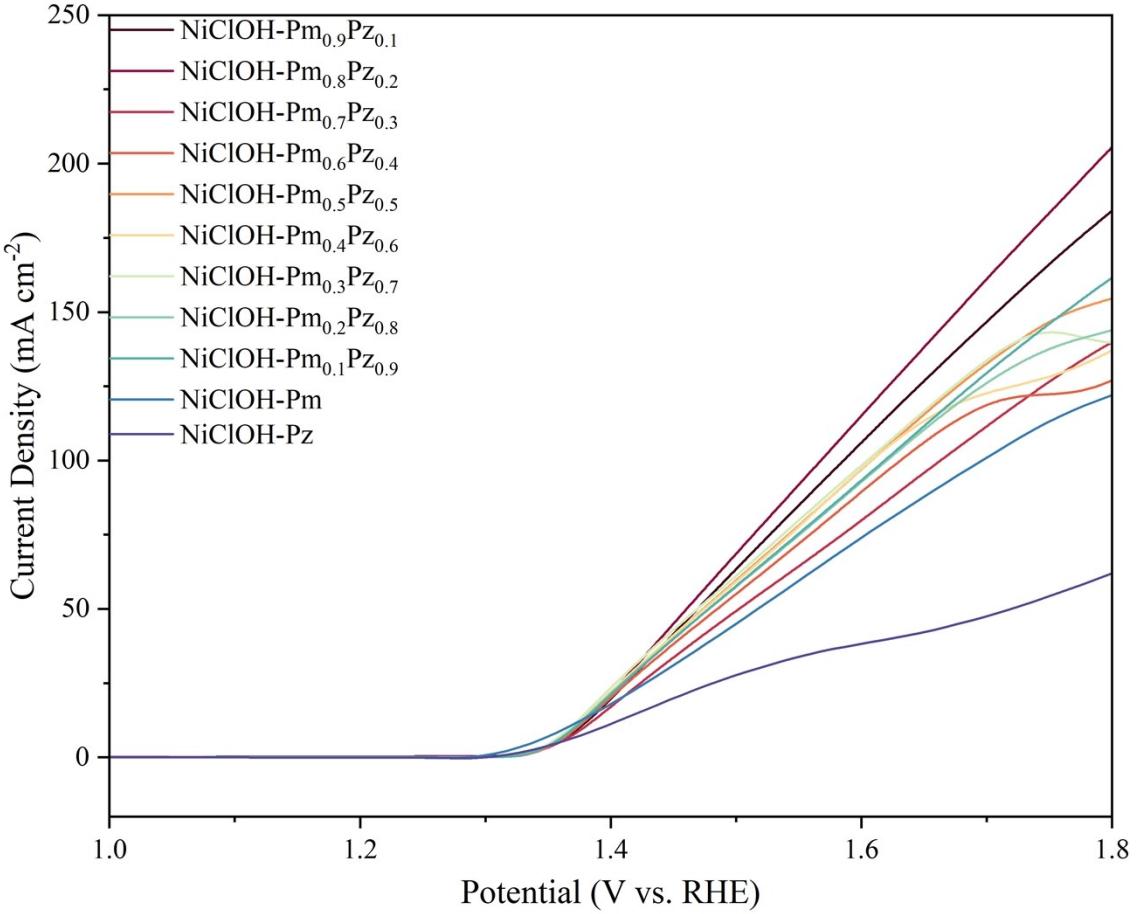

Figure S8. Polarization curves for UOR with NiClOH-Pm_xPz_{1-x} samples with different ligand ratios compared to reference NiClOH-Pm and NiClOH-Pz.

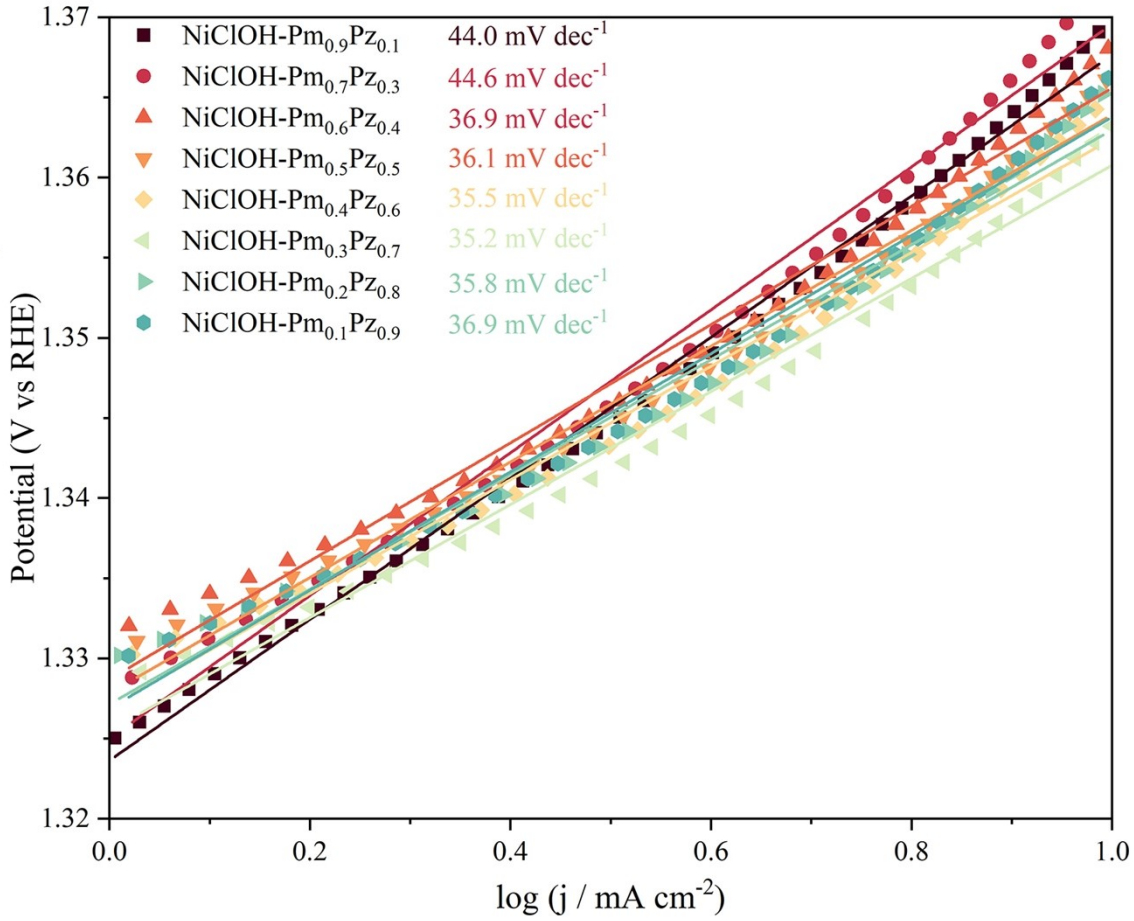

Figure S9. Tafel plots for different Pm/Pz ratios of ligand substituted samples of NiClOH-Pm_xPz_{1-x}.

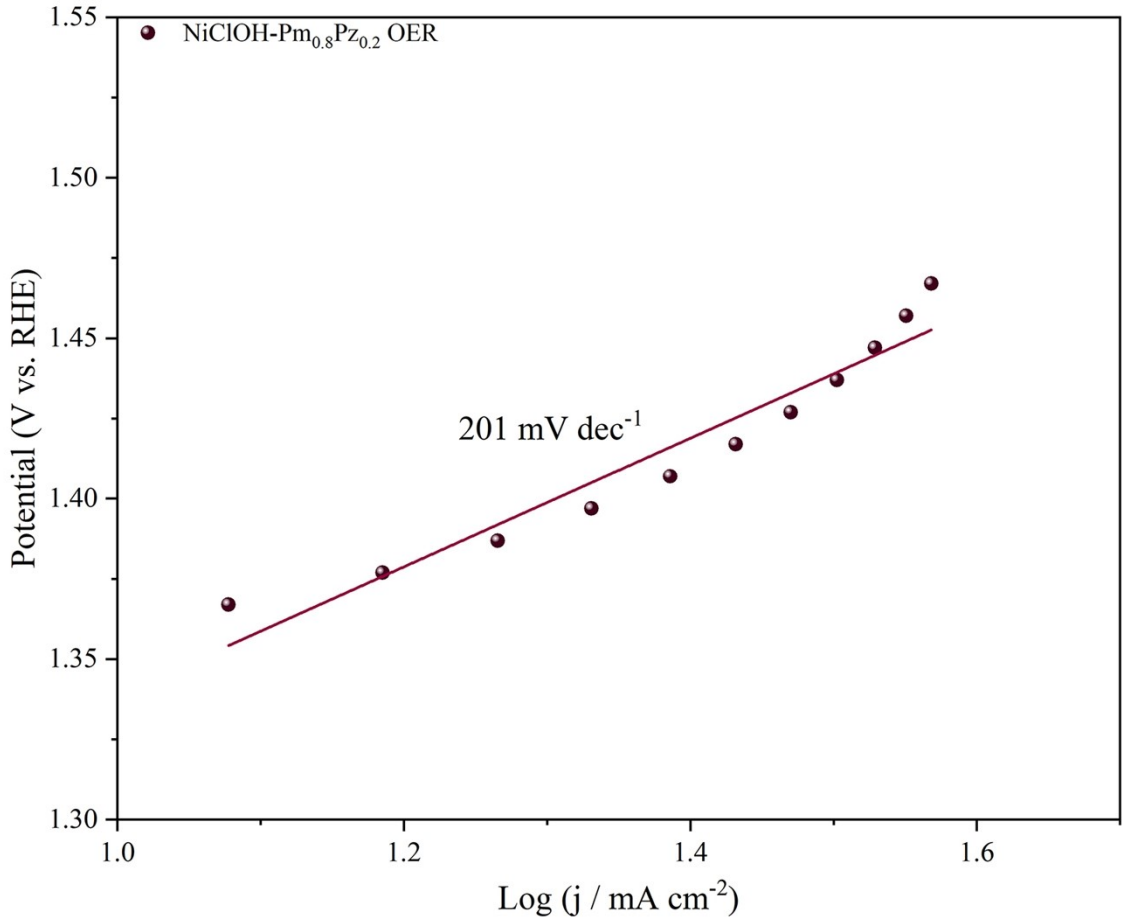

Figure S10. Tafel plot of NiClOH-$Pm_{0.8}Pz_{0.2}$ in 1 M KOH electrolyte without urea.

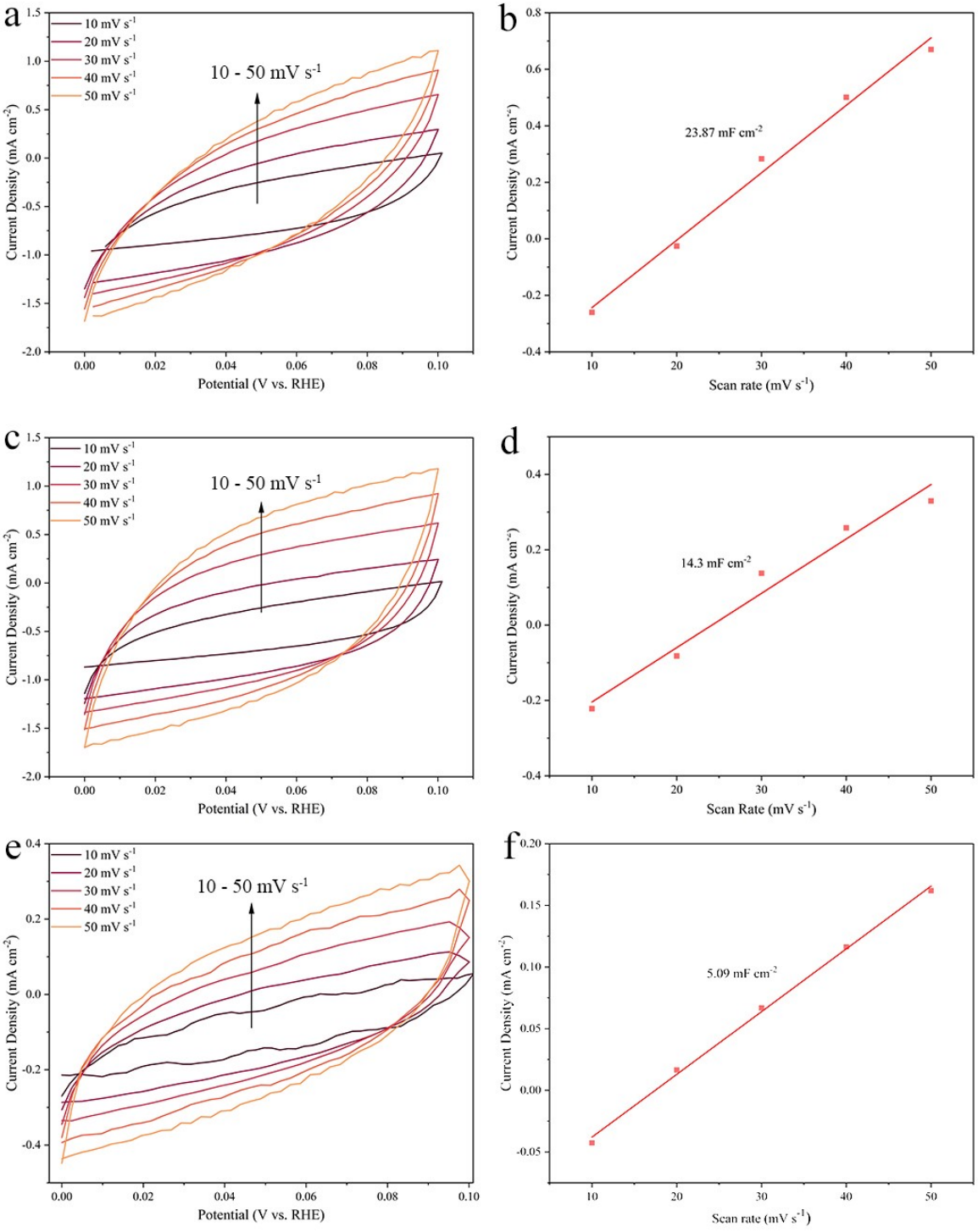

Figure S11. (a, c, d) Electrochemical double layer capacitance curves of NiClOH-$Pm_{0.8}Pz_{0.2}$, NiClOH-Pm, and NiClOH-Pz; (b, d, f) Current densities at 0.05 V *vs.* scan rates for the different samples.

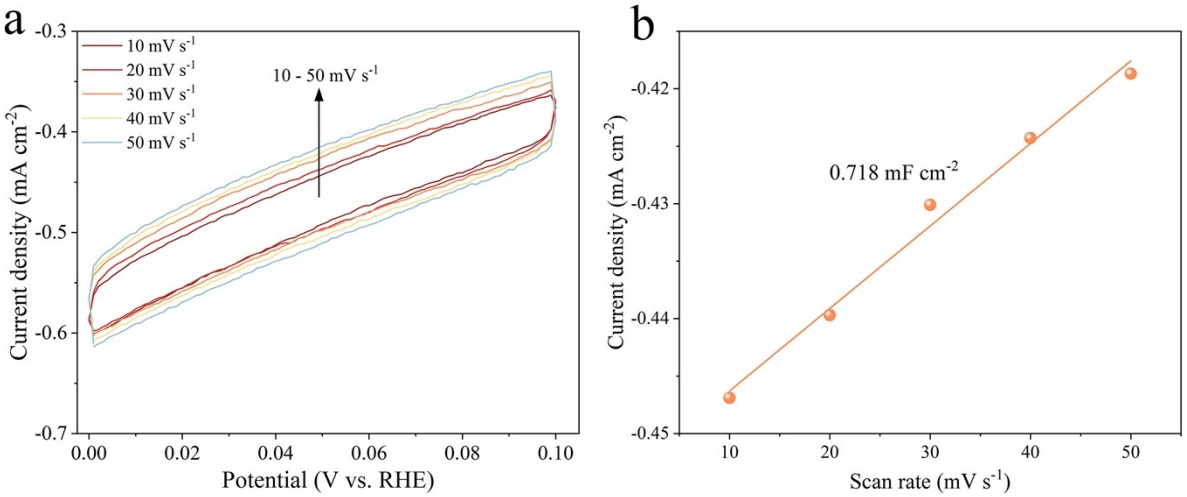

Figure S12. (a) Electrochemical double layer capacitance curves of $Ni(OH)_2$; (b) Current densities at 0.05 V *vs.* scan rates.

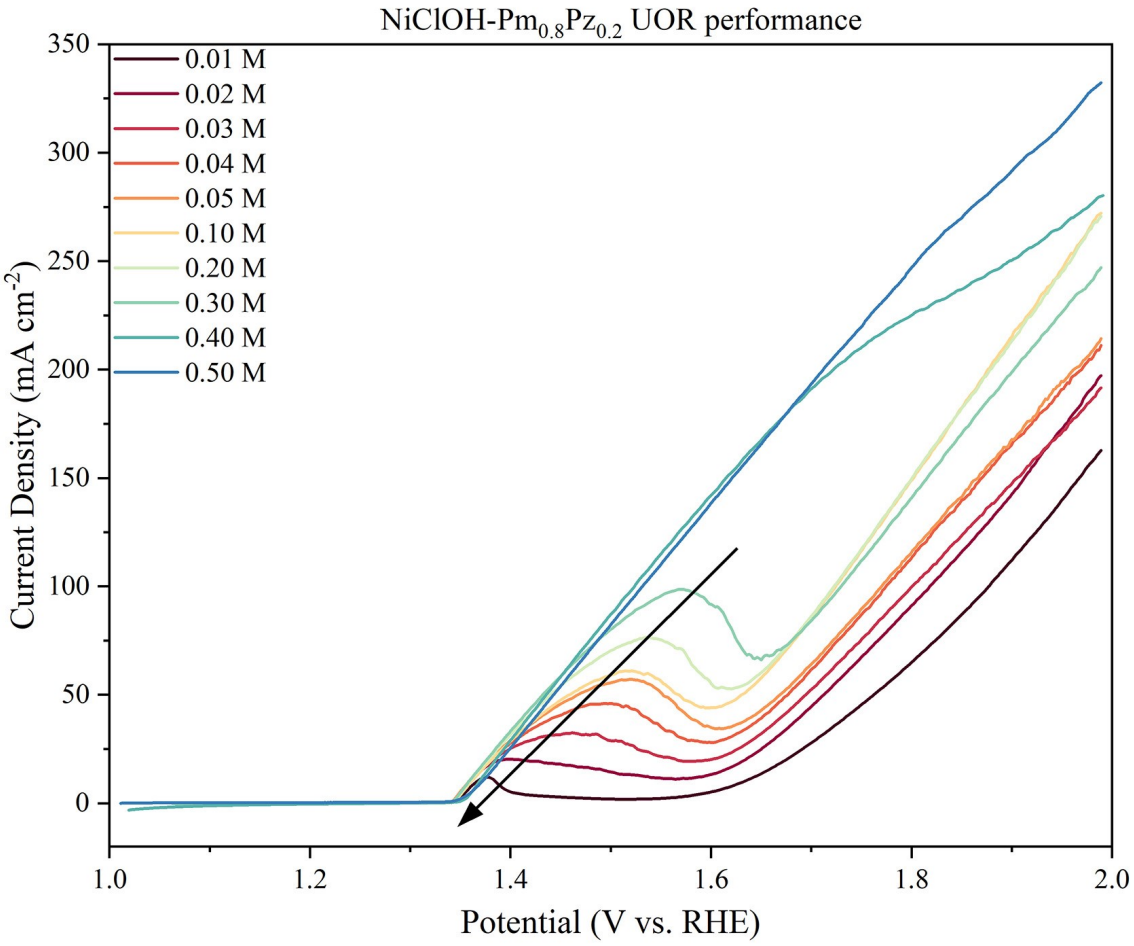

Figure S13. LSV curves of NiClOH-$Pm_{0.8}Pz_{0.2}$ hybrid materials under different urea concentrations.

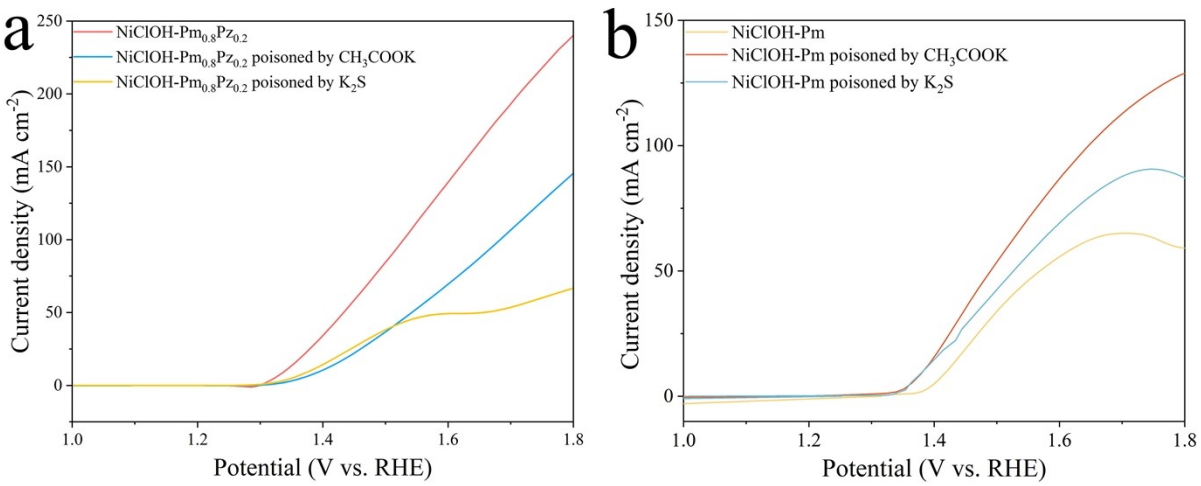

Figure S14. LSV curves of (a) NiClOH-$Pm_{0.8}Pz_{0.2}$ and (b) NiClOH-Pm (red line), potassium acetate (blue line) and potassium sulfide (yellow line) poisoned NiClOH-$Pm_{0.8}Pz_{0.2}$ in 1 M KOH + 0.5 M urea.

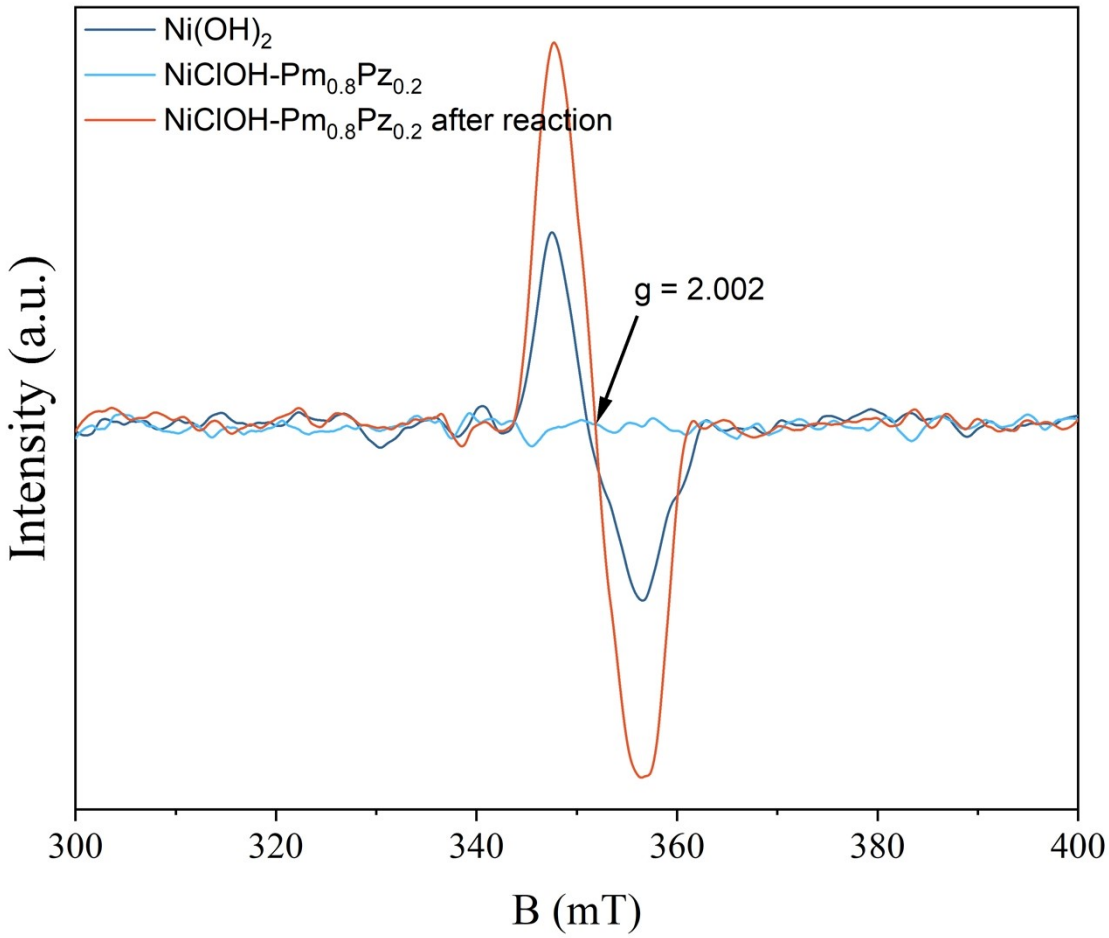

Figure S15. EPR spectra of NiClOH-$Pm_{0.8}Pz_{0.2}$ before and after long-term UOR testing vs. $Ni(OH)_2$ as a reference.

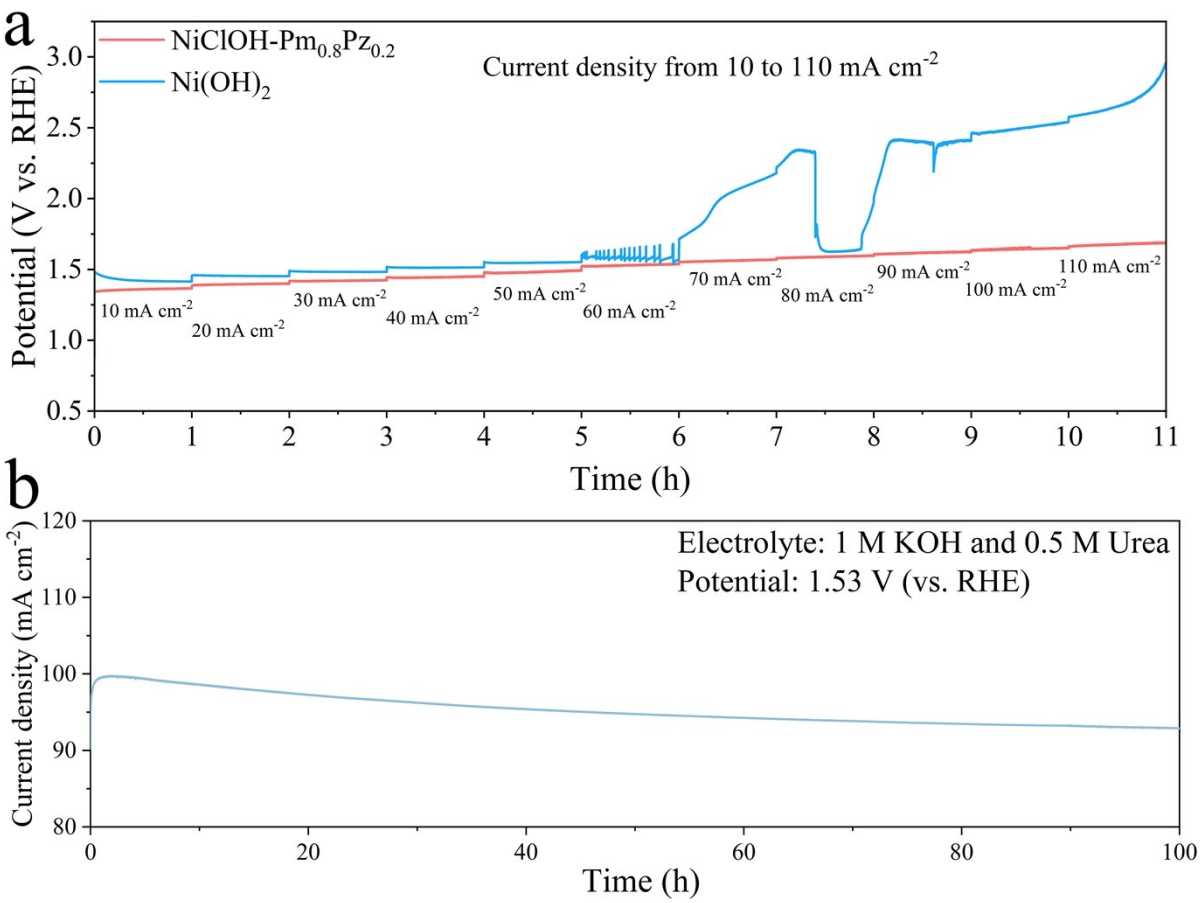

Figure S16. (a) Chronopotentiometry test of $Ni(OH)_2$ and NiClOH-$Pm_{0.8}Pz_{0.2}$ at current densities from 10 to 110 mA cm^{-2} for 11 h; (b) chronoamperometry test of NiClOH-$Pm_{0.8}Pz_{0.2}$ at 1.53 V (vs. RHE) for 100 h.

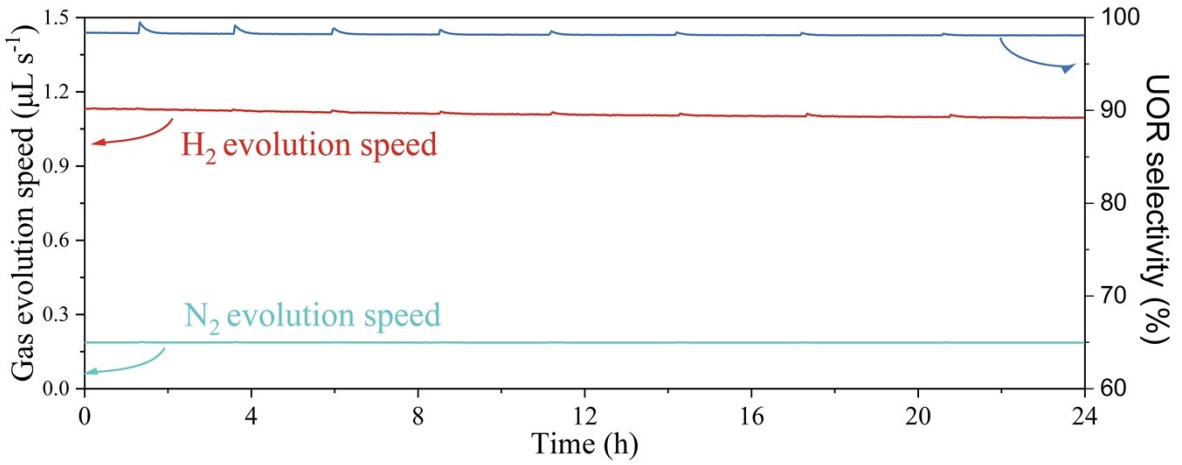

Figure S17. H_2 and N_2 evolution speed calculated from GC data and UOR selectivity for NiClOH-$Pm_{0.8}Pz_{0.2}$.

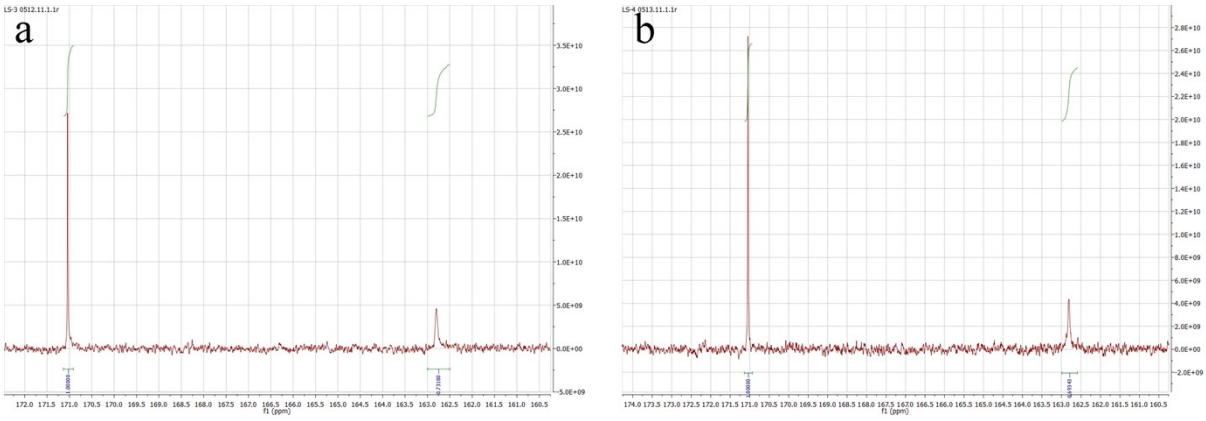

Figure S18. ^{13}C NMR spectrum of 1 M KOH and 0.5 M urea electrolyte (a) before and (b) after 24 h of testing.

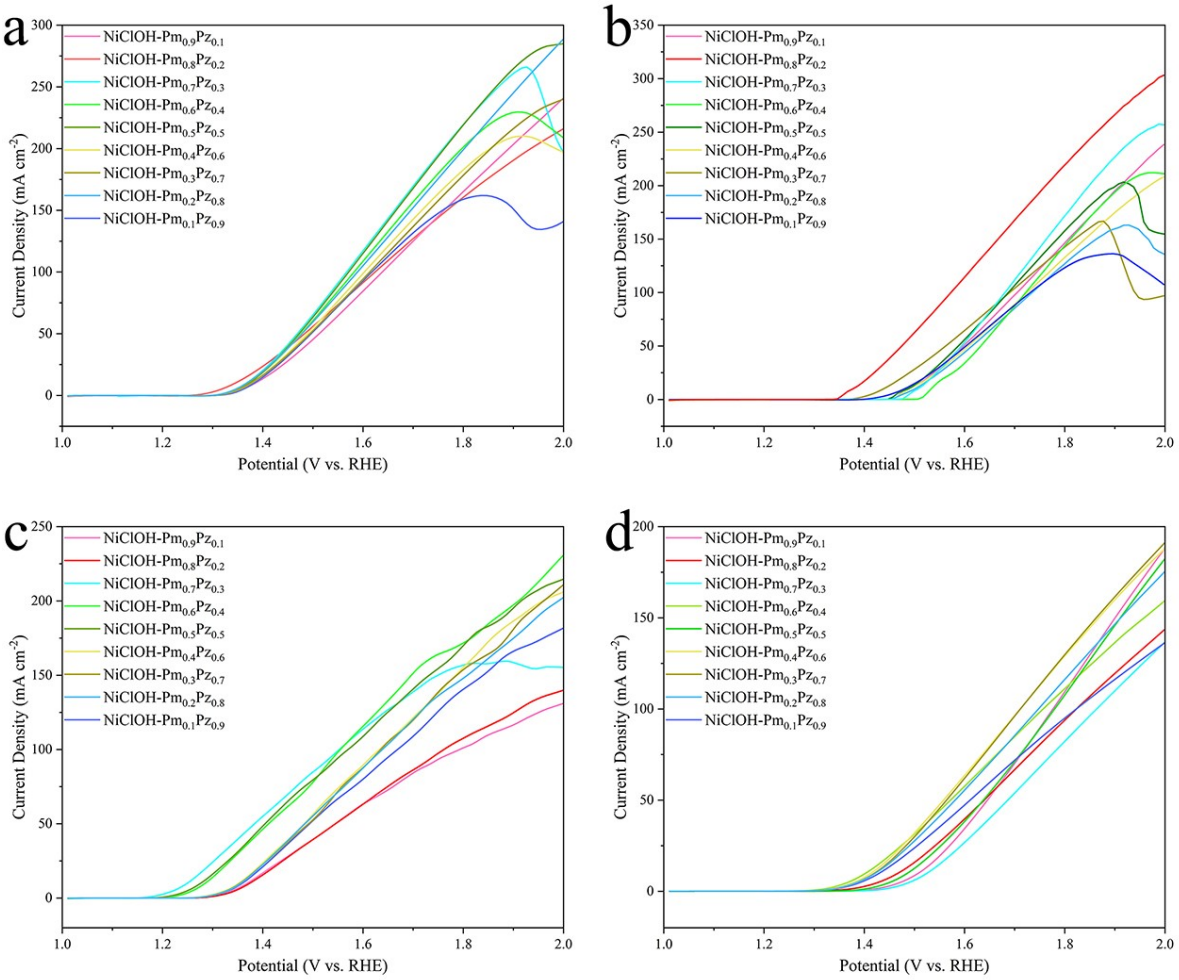

Figure S19. LSV curves of NiClOH-$Pm_{0.8}Pz_{0.2}$ hybrid materials evaluated with 1 M KOH and 0.5 M biomass for different oxidation reactions: (a) methanol, (b) ethanol, (c) benzyl alcohol, (d) glycerin.

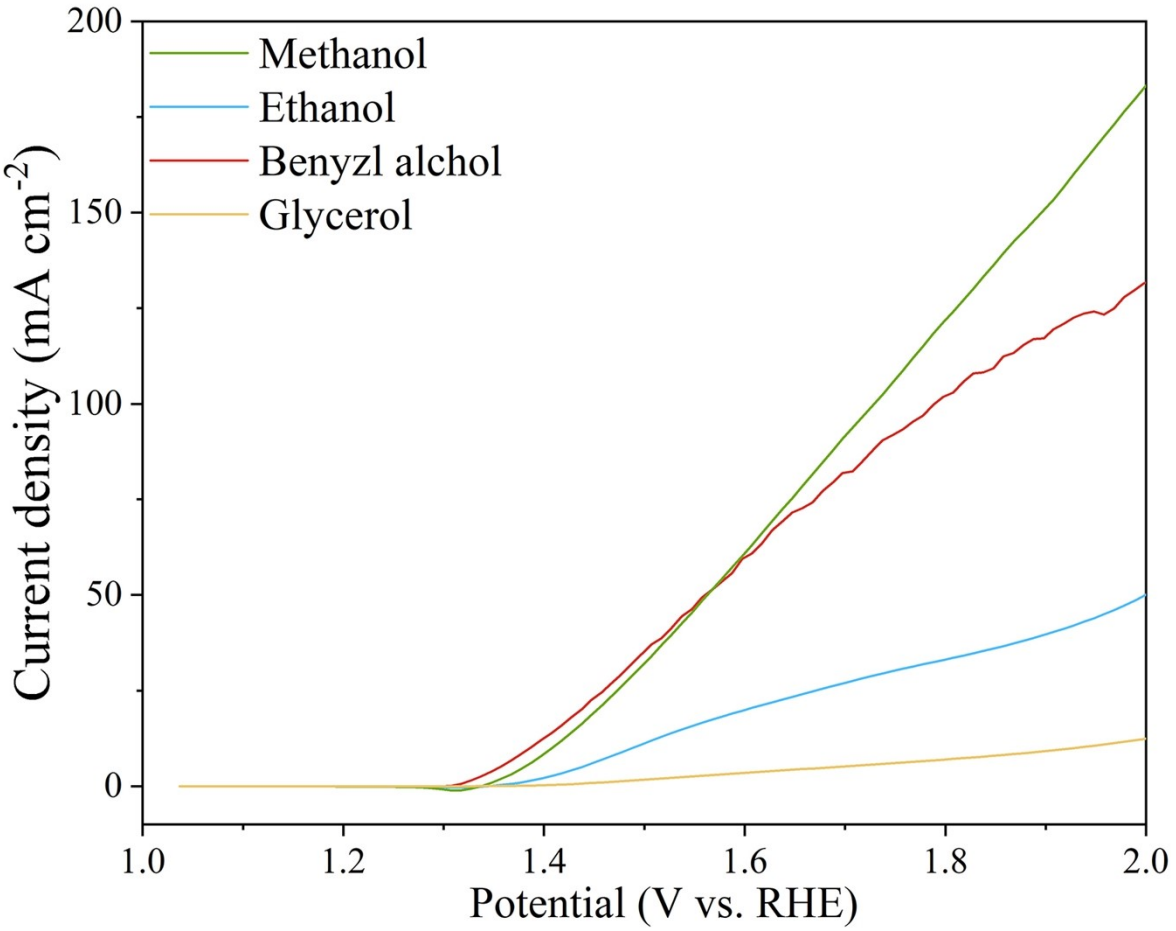

Figure S20. LSV curves of $Ni(OH)_2$ tested with 1 M KOH and 0.5 M biomass for different oxidation reactions (methanol, ethanol, benzyl alcohol, and glycerin).

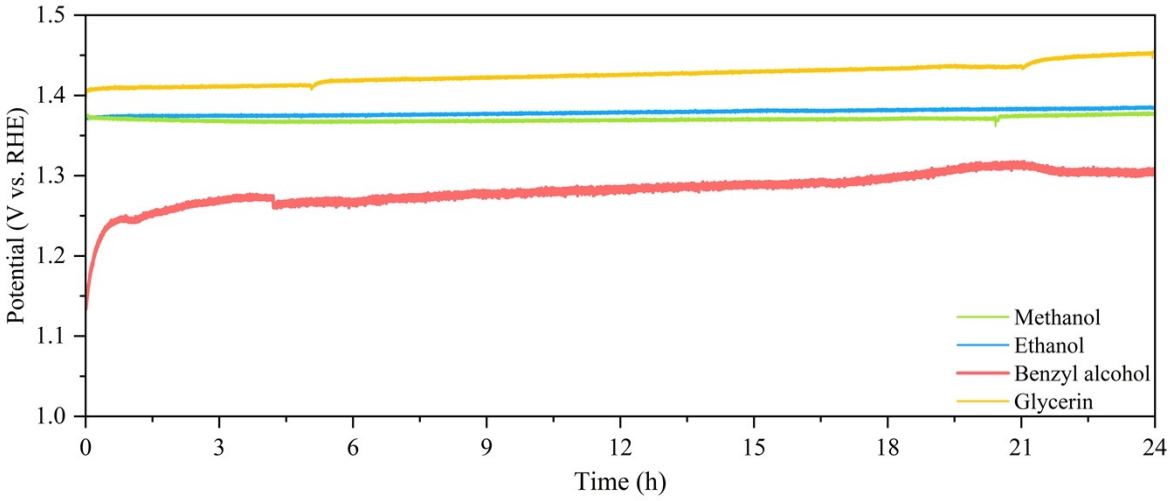

Figure S21. Long-term electrocatalysis tests in 1 M KOH and 0.5 M biomass at a current density of 10 mA cm^{-2} (green, methanol; blue, ethanol; red, benzyl alcohol; yellow, glycerin).

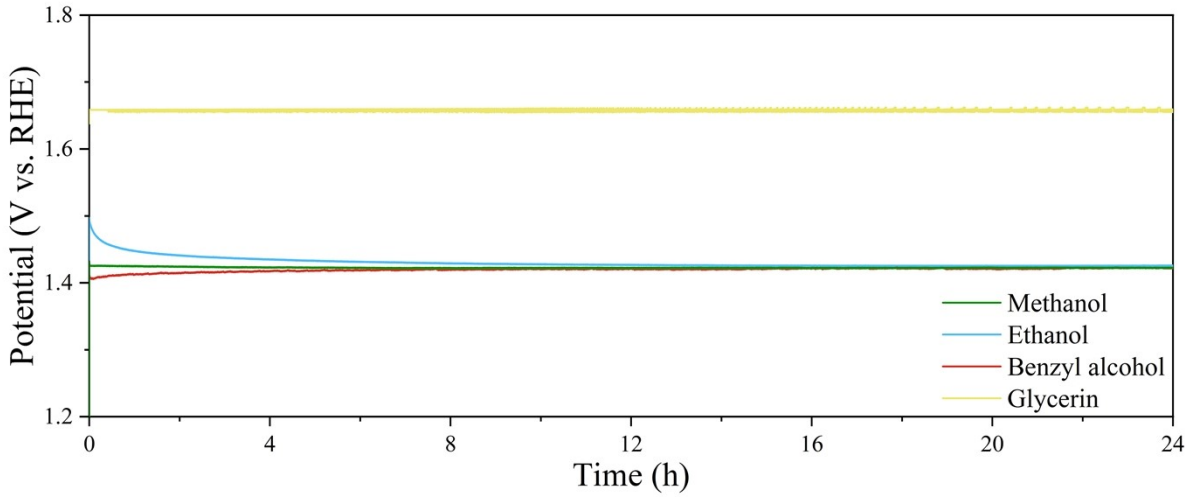

Figure S22. Long-term electrocatalysis tests in 1 M KOH and 0.5 M biomass of $Ni(OH)_2$ electrocatalyst at a current density of 10 mA cm^{-2} (green, methanol; blue, ethanol; red, benzyl alcohol; yellow, glycerin).

S2.3 Post-catalytic characterizations (Figures S22 – S31)

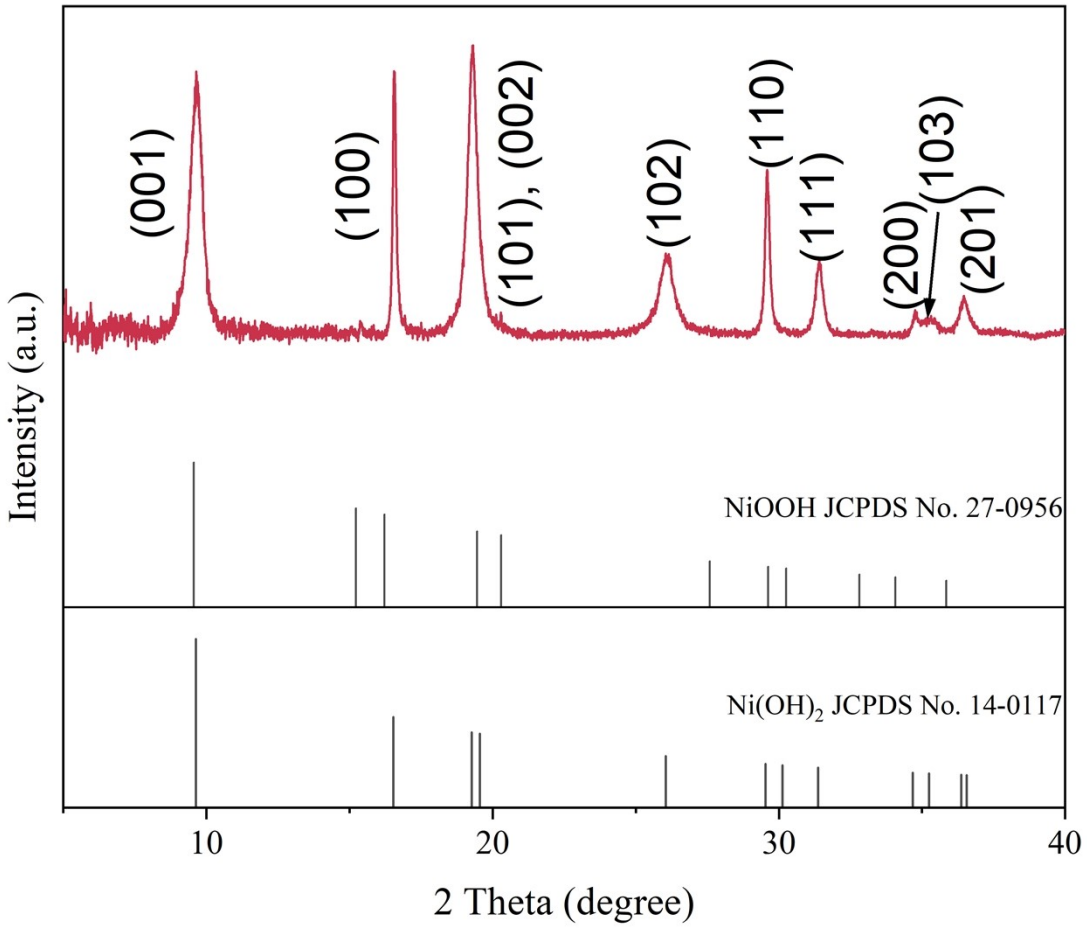

Figure S23. XRD pattern of NiClOH-$Pm_{0.8}Pz_{0.2}$ after 24 h of UOR testing.

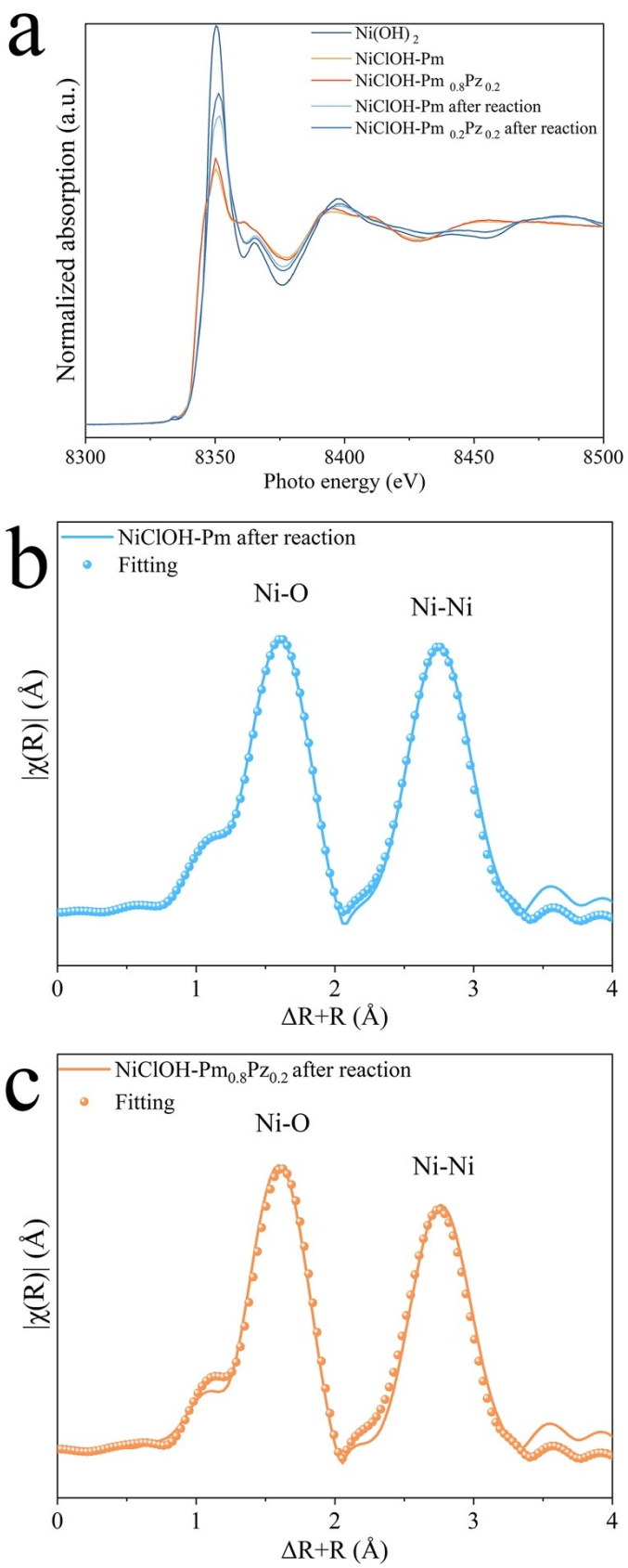

Figure S24. (a) XANES spectra of metal $Ni(OH)_2$, NiClOH-Pm (before and after UOR) and NiClOH-$Pm_{0.8}Pz_{0.2}$ (before and after UOR). (b, c) EXAFS spectra of NiClOH-Pm and NiClOH-$Pm_{0.8}Pz_{0.2}$ after 24 h of UOR testing.

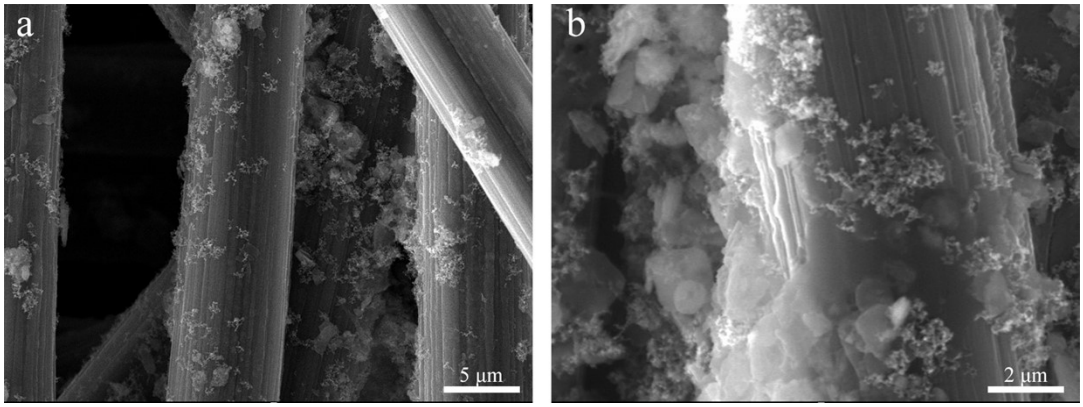

Figure S25. SEM images of NiClOH-$Pm_{0.8}Pz_{0.2}$ on CP after 24 h of UOR testing.

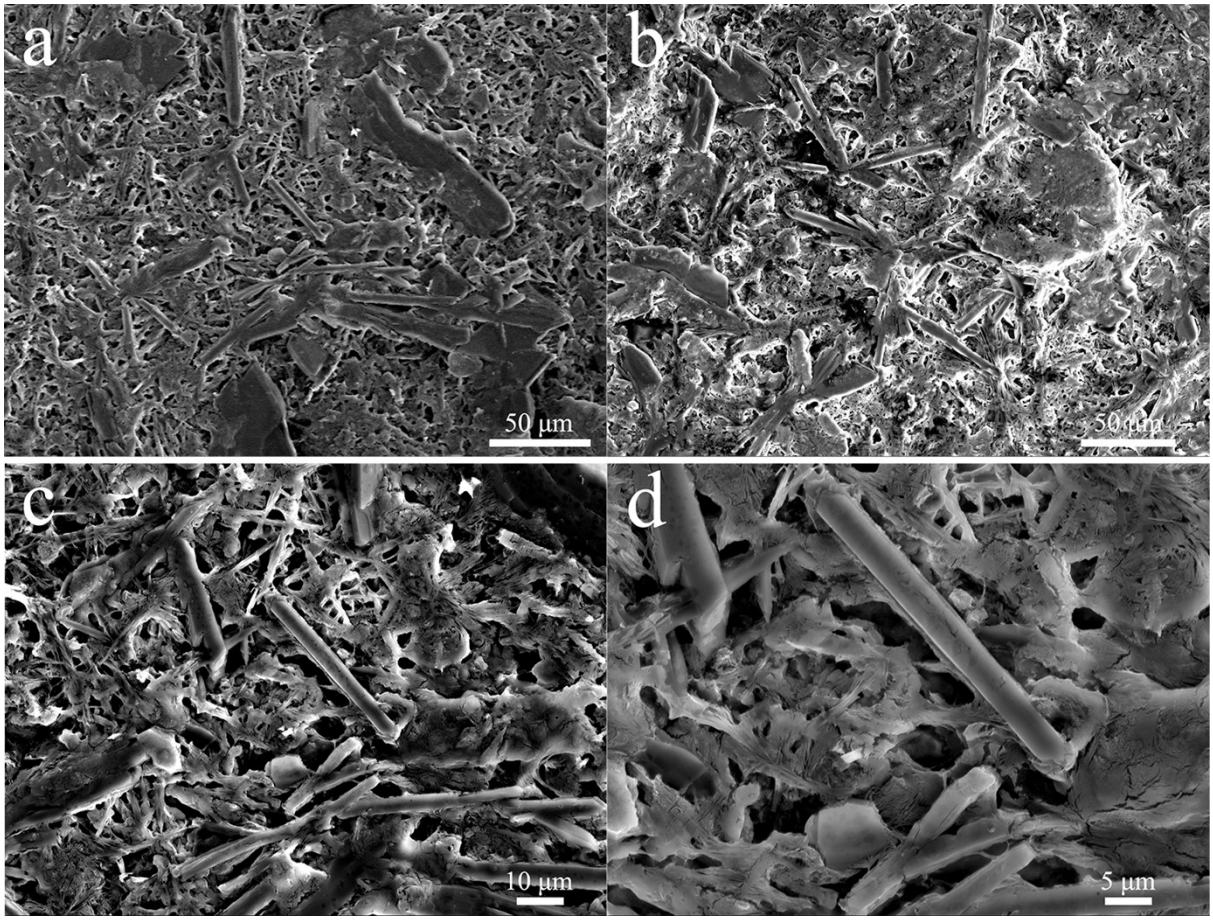

Figure S26. SEM images of NiClOH-$Pm_{0.8}Pz_{0.2}$ powder after 24 h of UOR testing.

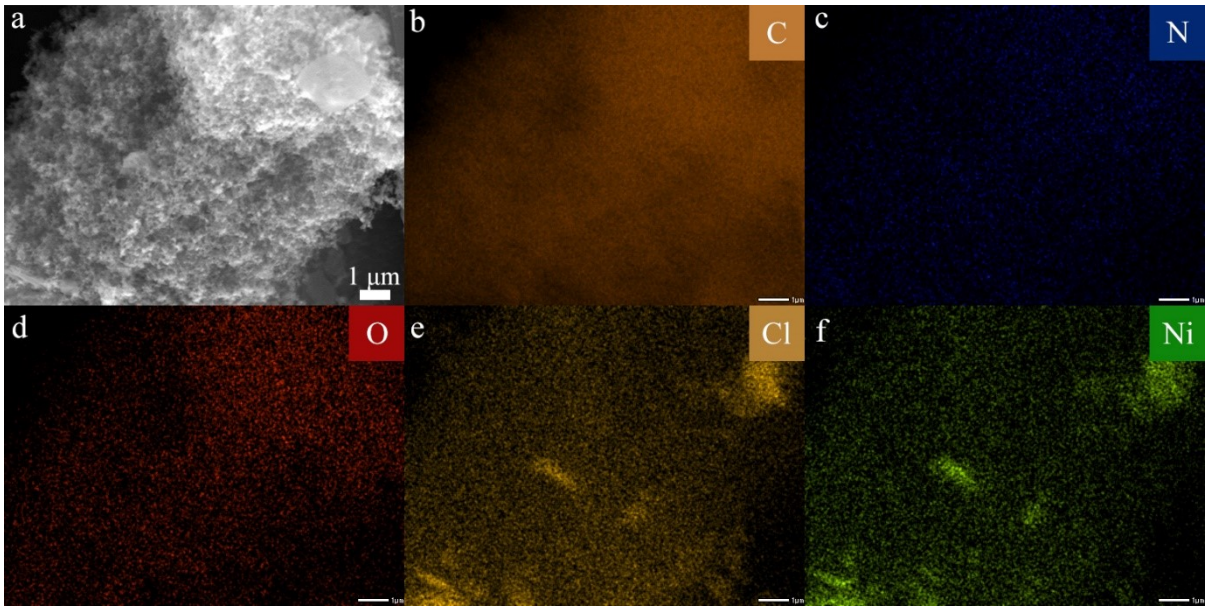

Figure S27. (a) SEM image of NiClOH-$Pm_{0.8}Pz_{0.2}$ on CP after 24 h of UOR testing (b) EDX mapping with (b) C, (c) N, (d) O, (e) Cl, and (f) Ni.

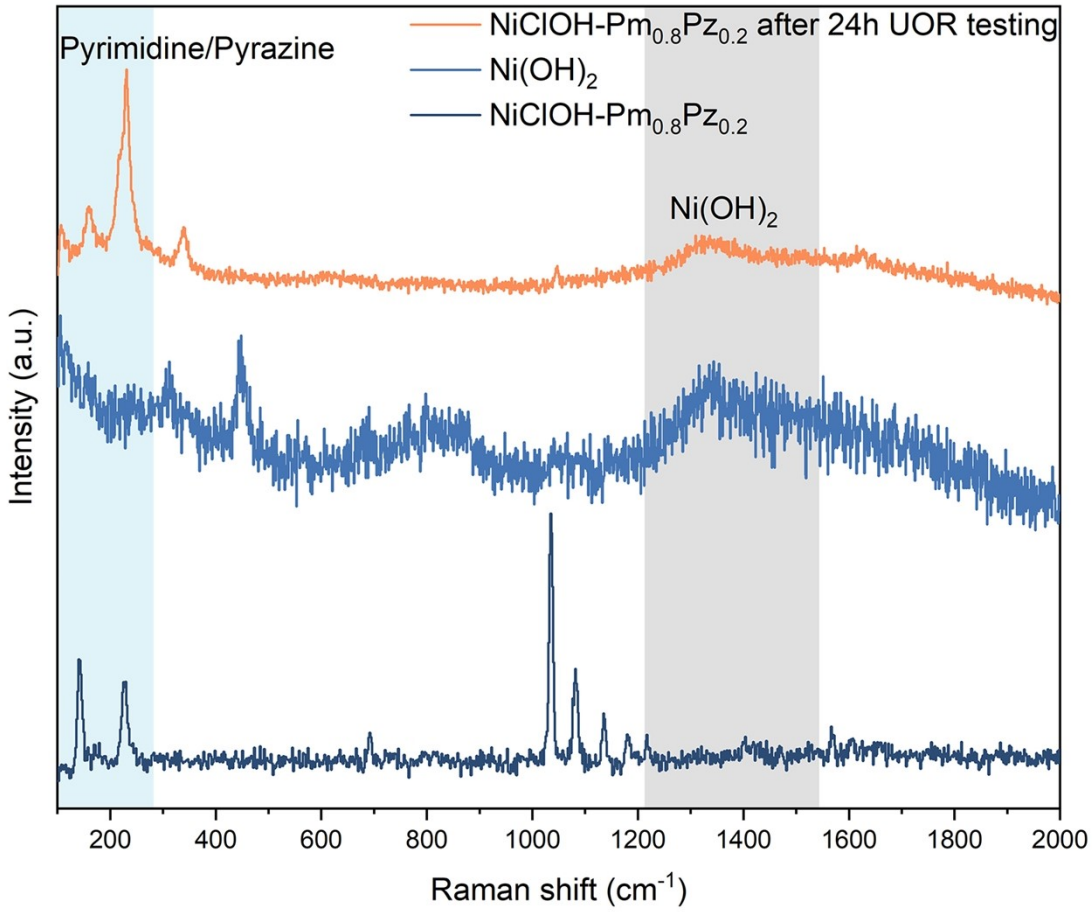

Figure S28. Raman spectra of NiClOH-$Pm_{0.8}Pz_{0.2}$ powder after 24 h of UOR testing.

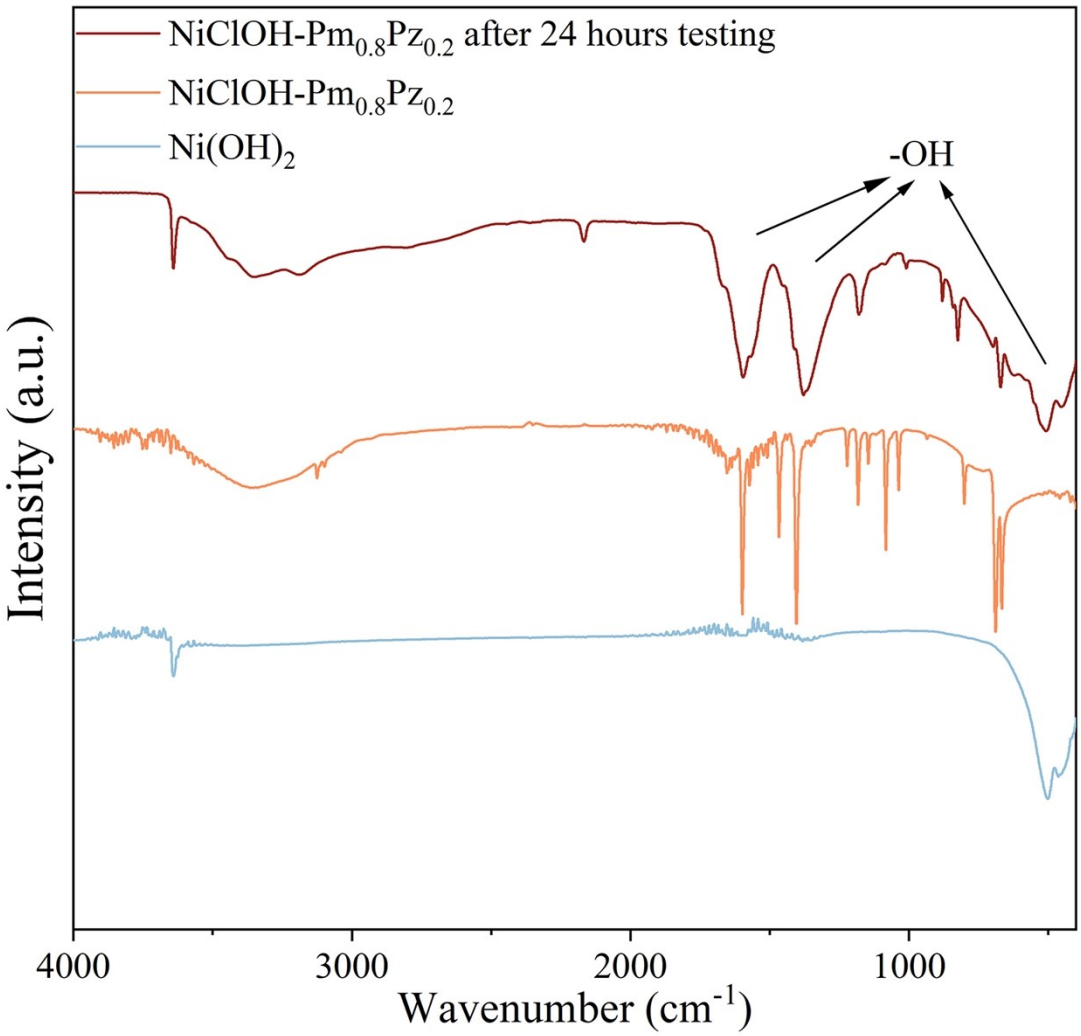

Figure S29. FT-IR spectra of NiClOH-$Pm_{0.8}Pz_{0.2}$ after 24 h of UOR testing.

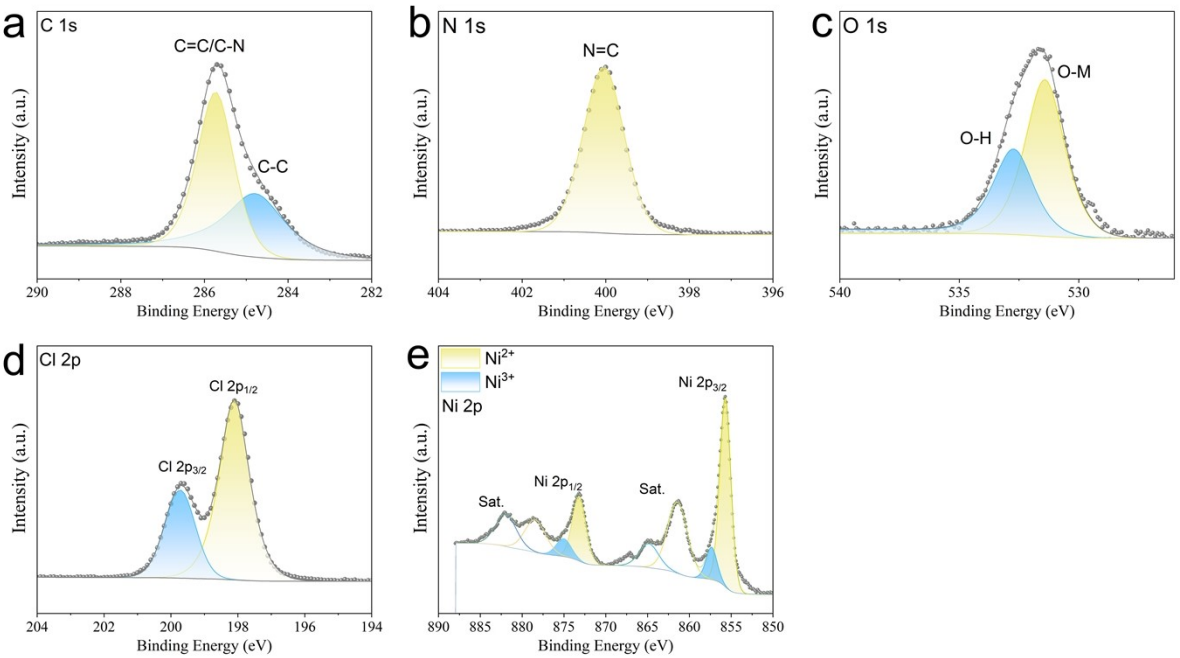

Figure S30. (a) C 1s, (b) N 1s, (c) O 1s, (d) Cl 2p, and (e) Ni 2p XP spectra of NiClOH-$Pm_{0.8}Pz_{0.2}$ after a long-term 24 h UOR test.

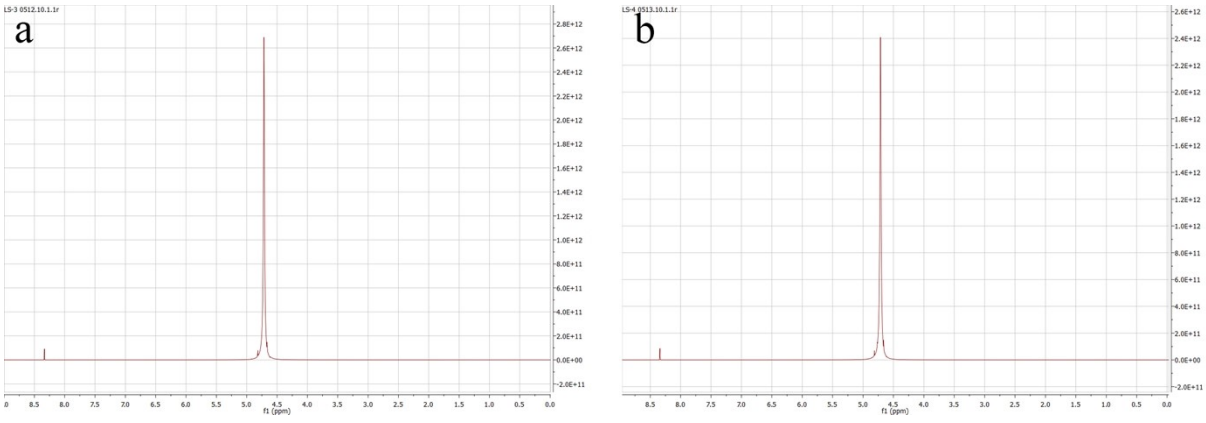

Figure S31. ^{1}H NMR spectrum of 1 M KOH and 0.5 M urea electrolyte (a) before and (b) after 24 h testing.

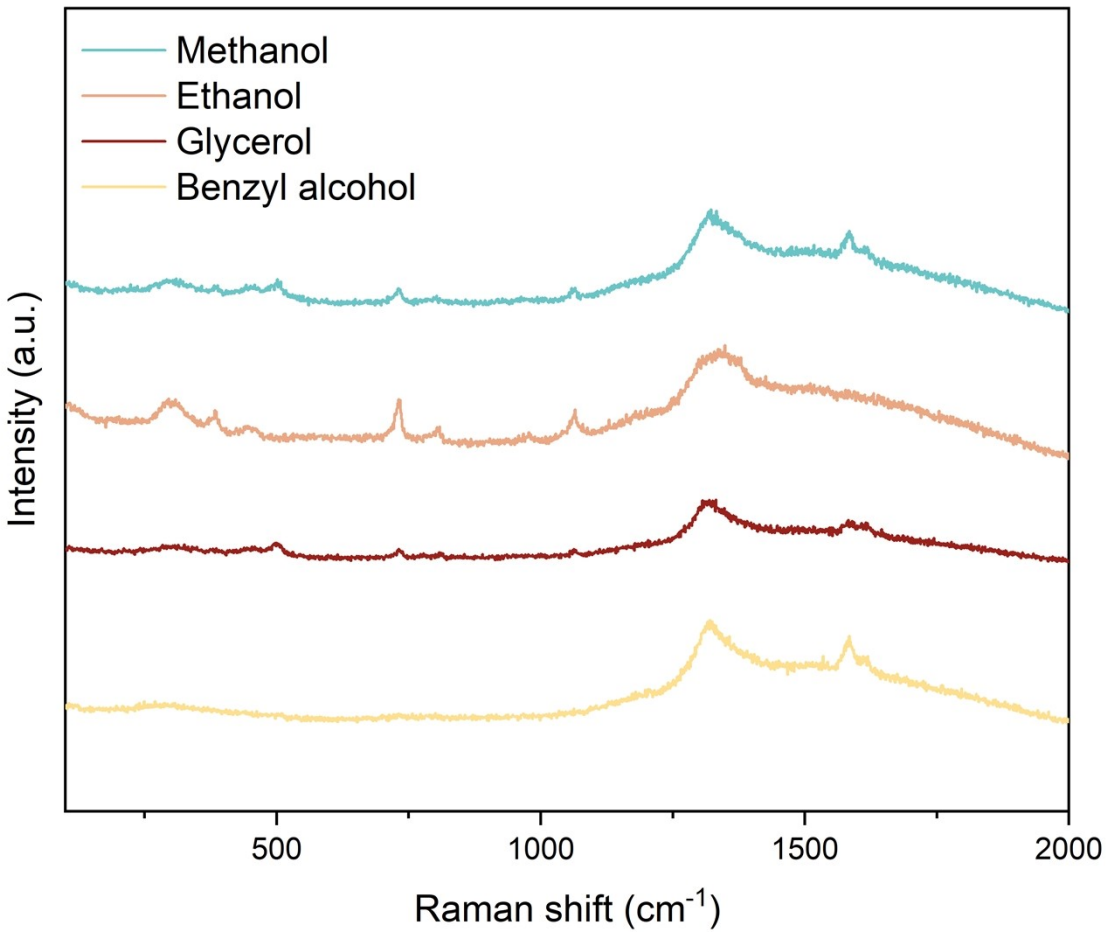

Figure S32. Raman spectra of NiClOH-$Pm_{0.8}Pz_{0.2}$ powder after 24 h testing of biomass methanol, ethanol, glycerol and benzyl alcohol oxidation reactions.

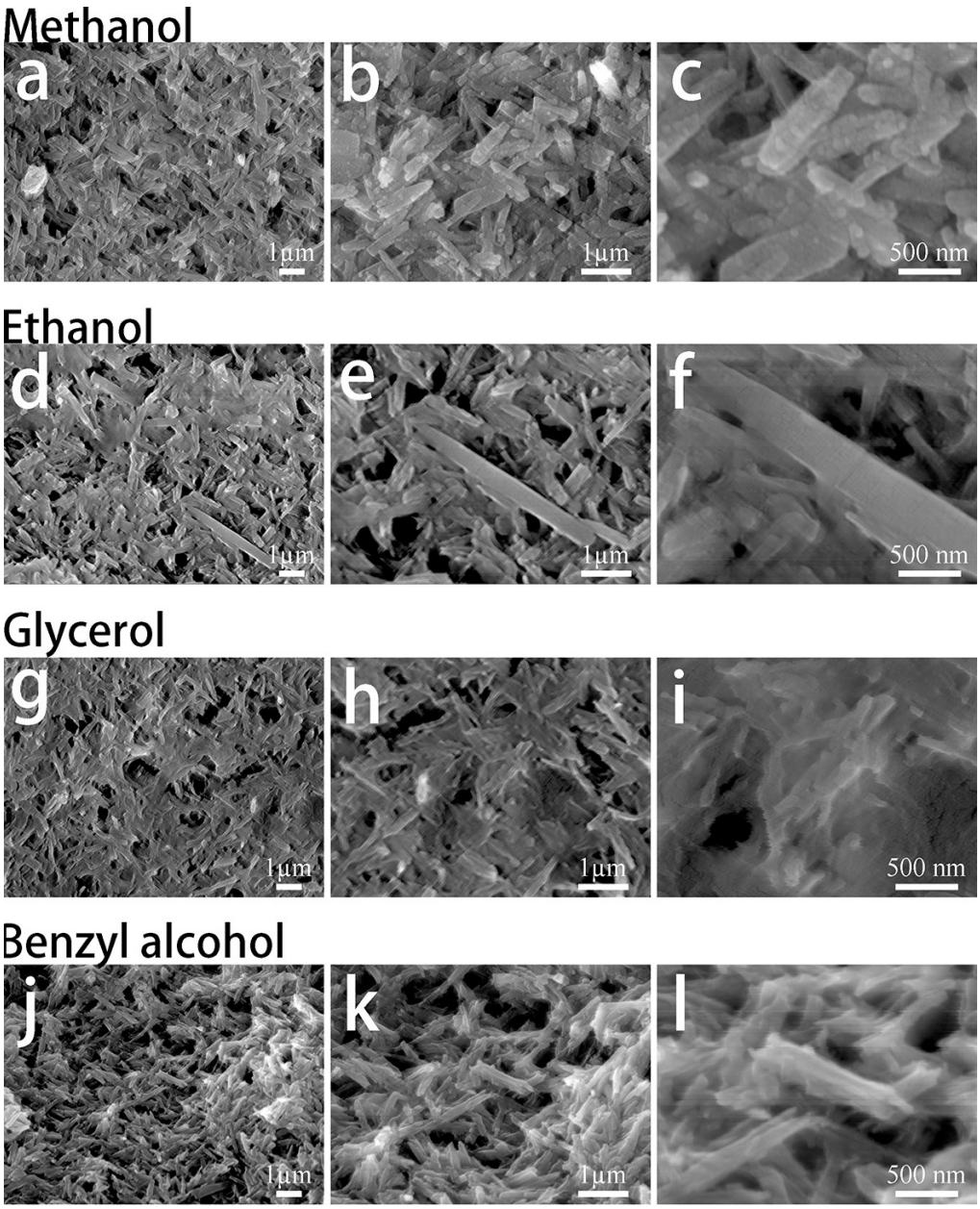

Figure S33. SEM images of NiClOH-$Pm_{0.8}Pz_{0.2}$ on CP after 24 h of testing in 1 M KOH and 0.5 M (a, b, and c) methanol, (d, e, f) ethanol, (g, h, i) glycerin, and (j, k, l) benzyl alcohol electrolyte.

S2.4 DFT calculations (Figures S32 – S41)

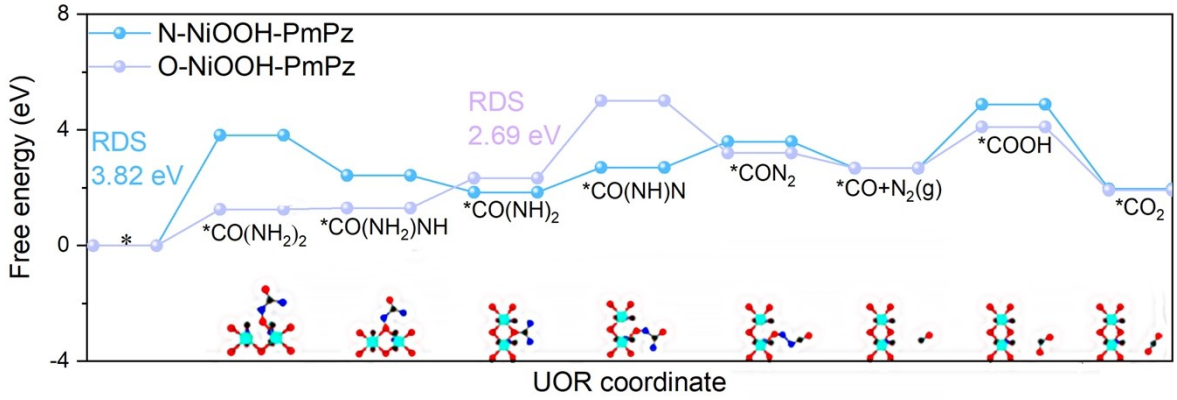

Figure S34. Free energy diagram of UOR with NiOOH-Pm-Pz without vacancies; N and O refer to nitrogen and oxygen atoms of urea absorbed on the surface of the hybrid catalyst, respectively.

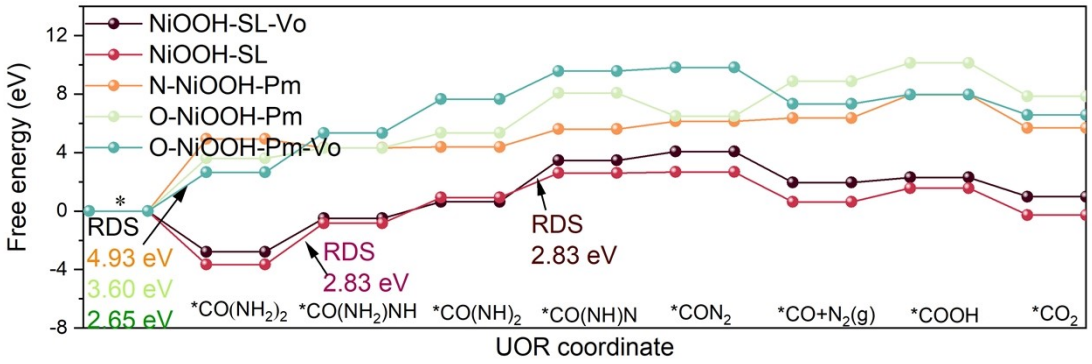

Figure S35. Free energy diagram of UOR with NiOOH single layer (SL) and NiOOH-Pm with and without vacancies, N and O refer to nitrogen and oxygen atoms of urea absorbed on the surface of hybrid catalysts, respectively.

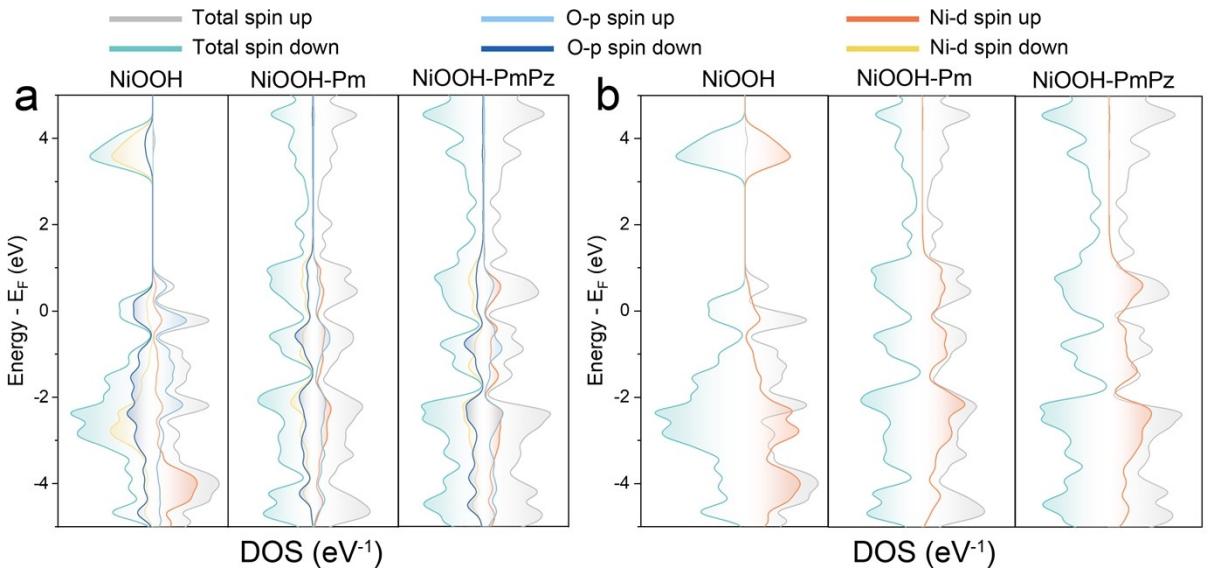

Figure S36. (a) Contribution of the Ni and O atoms to the electronic density on the surface layer, (b) contribution of the different Ni 3d dz^2 orbital to the DOS of the NiOOH single layer, NiOOH-Pm and NiOOH-PmPz without V_O (from left to right).

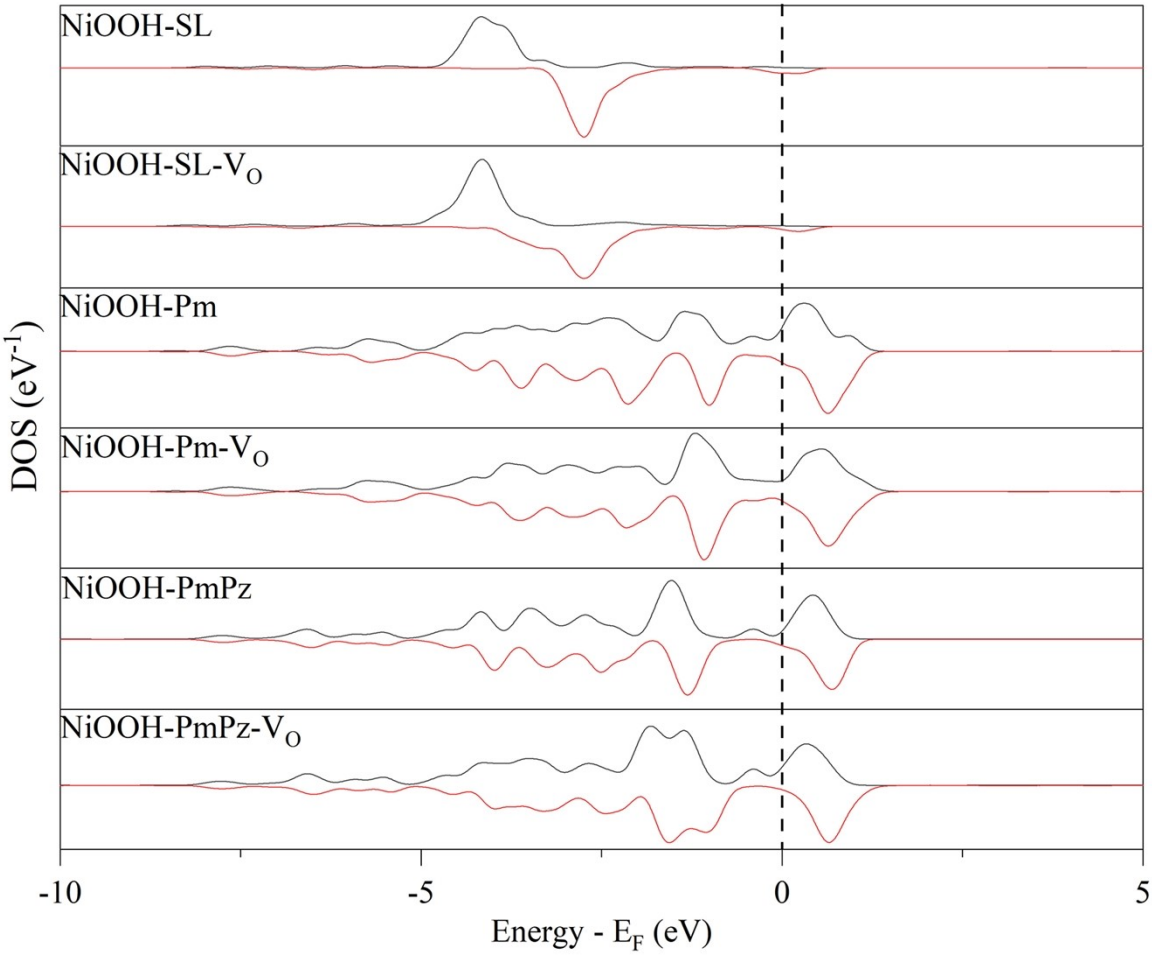

Figure S37. DOS of the Ni $3d_{z2}$ orbital calculated for the NiOOH surface that represents the active intermediate derived from post-catalytic $Ni(OH)_2$. From top to bottom: NiOOH without and with oxygen vacancies, NiOOH-Pm without and with vacancies, and NiOOH-PmPz without and with vacancies.

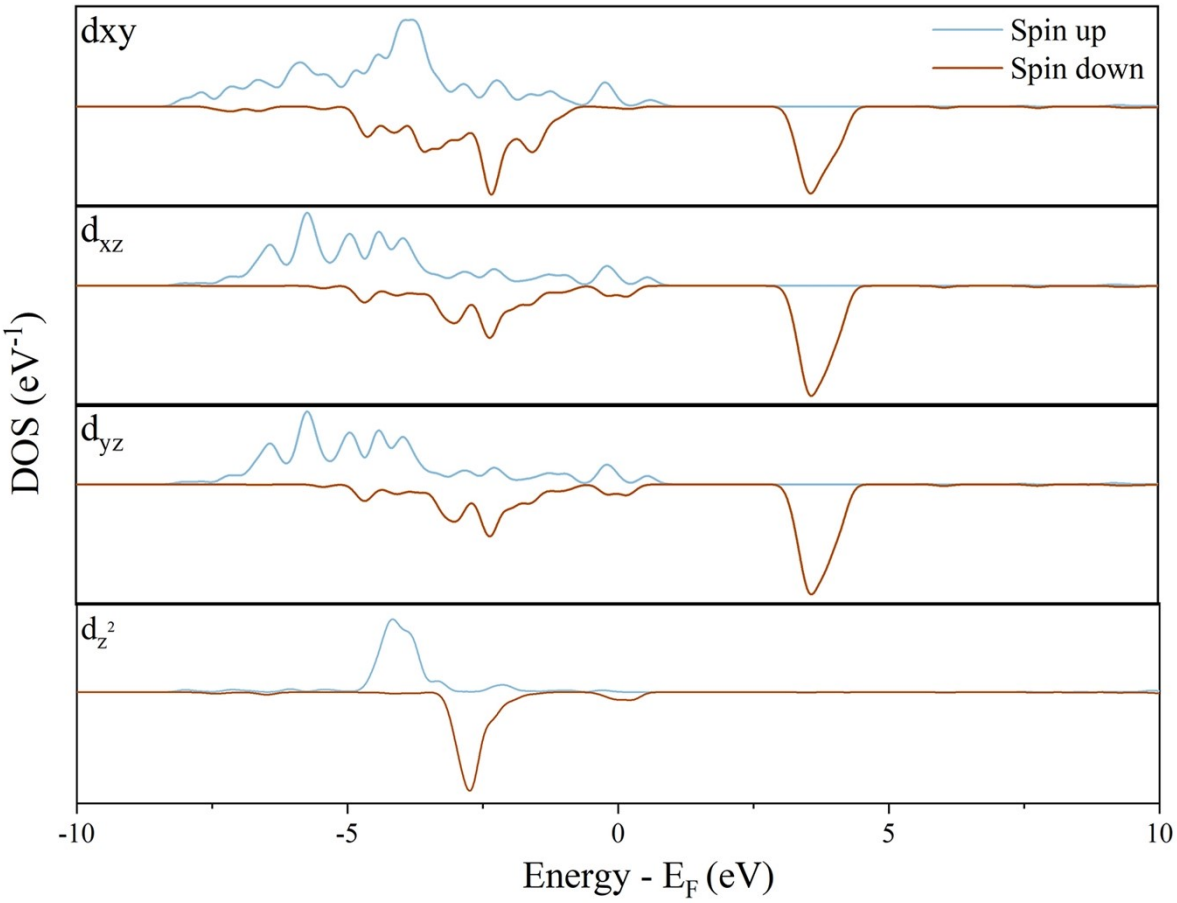

Figure S38. Contribution of different Ni 3d orbital directions on d_{xy}, d_{xz}, d_{yz}, and d_z^2 orbitals to the DOS of a NiOOH single layer without vacancies.

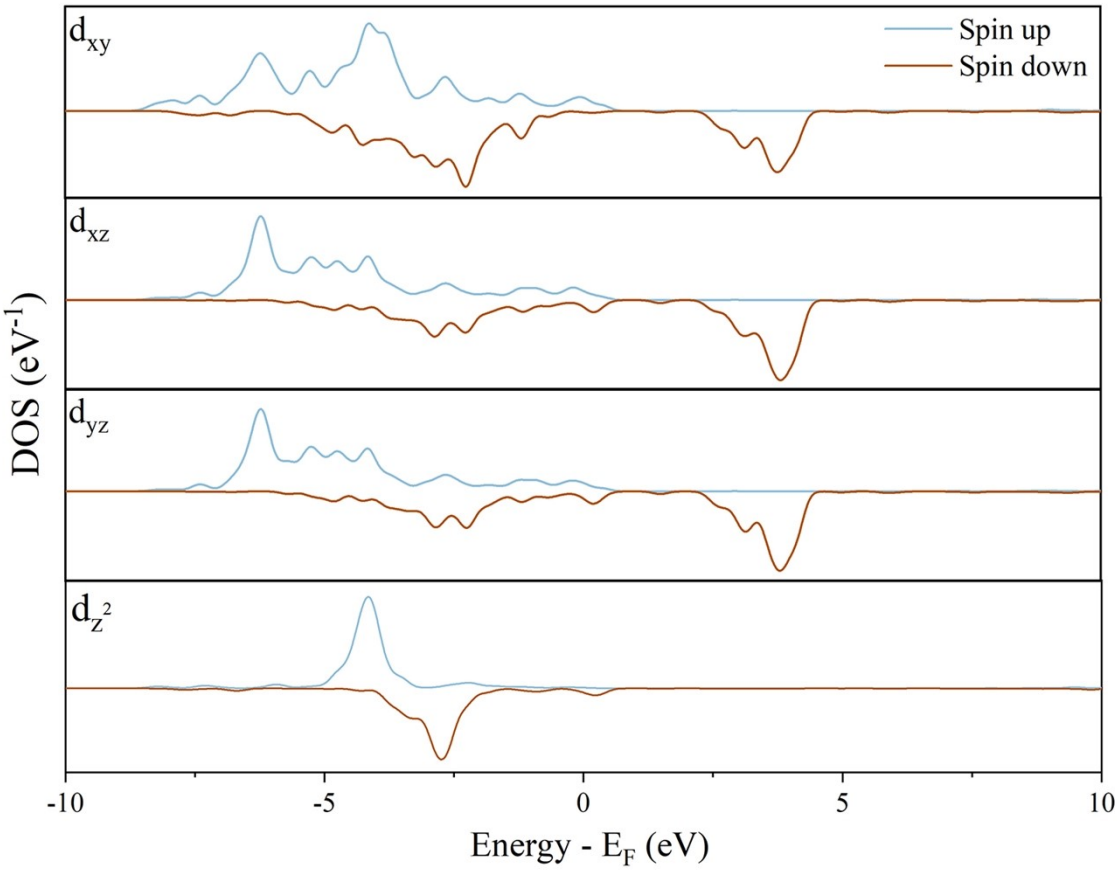

Figure S39. Contribution of different Ni 3d orbital directions on d_{xy}, d_{xz}, d_{yz}, and d_z^2 orbitals to the DOS of NiOOH-SL-Vo.

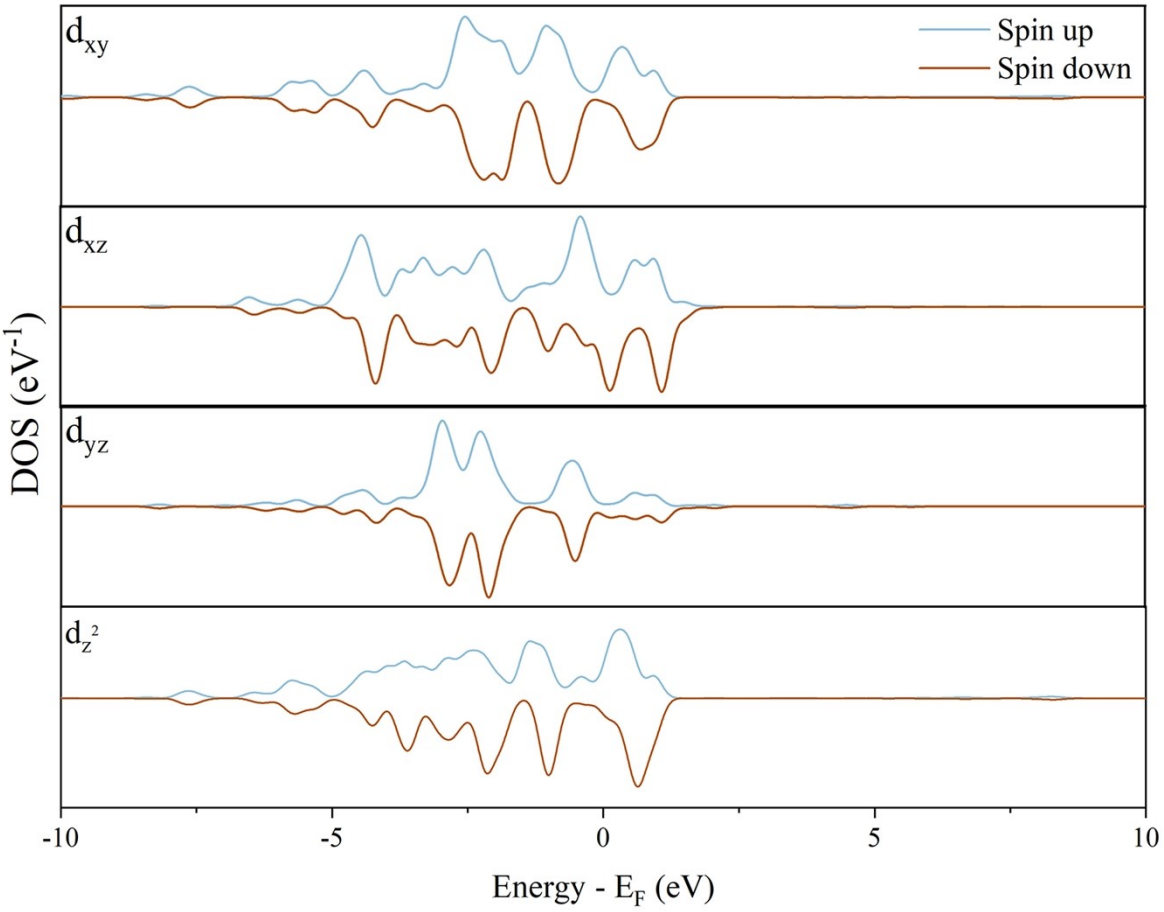

Figure S40. Contribution of different Ni 3d orbital directions on d_{xy}, d_{xz}, d_{yz}, and d_z^2 orbitals to the DOS of NiOOH-Pm.

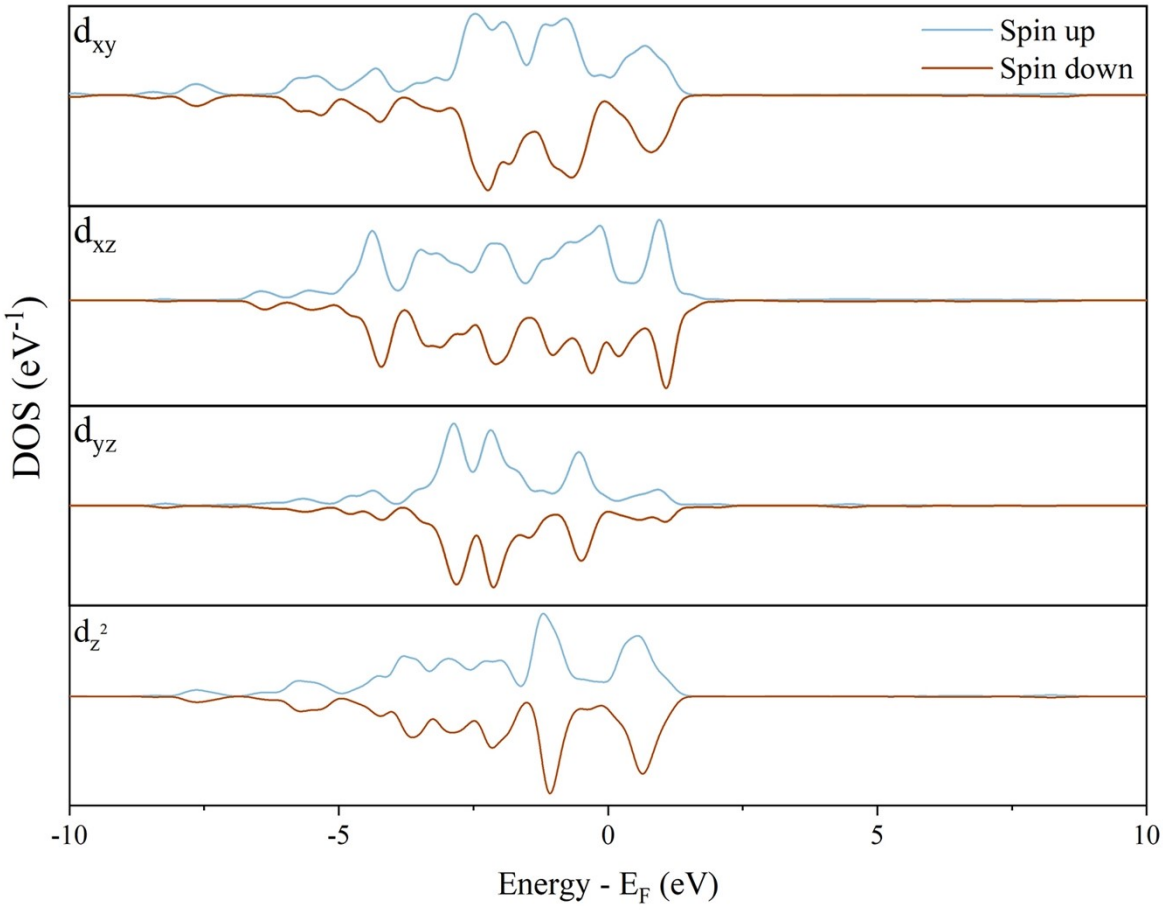

Figure S41. Contribution of different Ni 3d orbital directions on d_{xy}, d_{xz}, d_{yz}, and d_z^2 orbitals to the DOS of NiOOH-Pm-Vo.

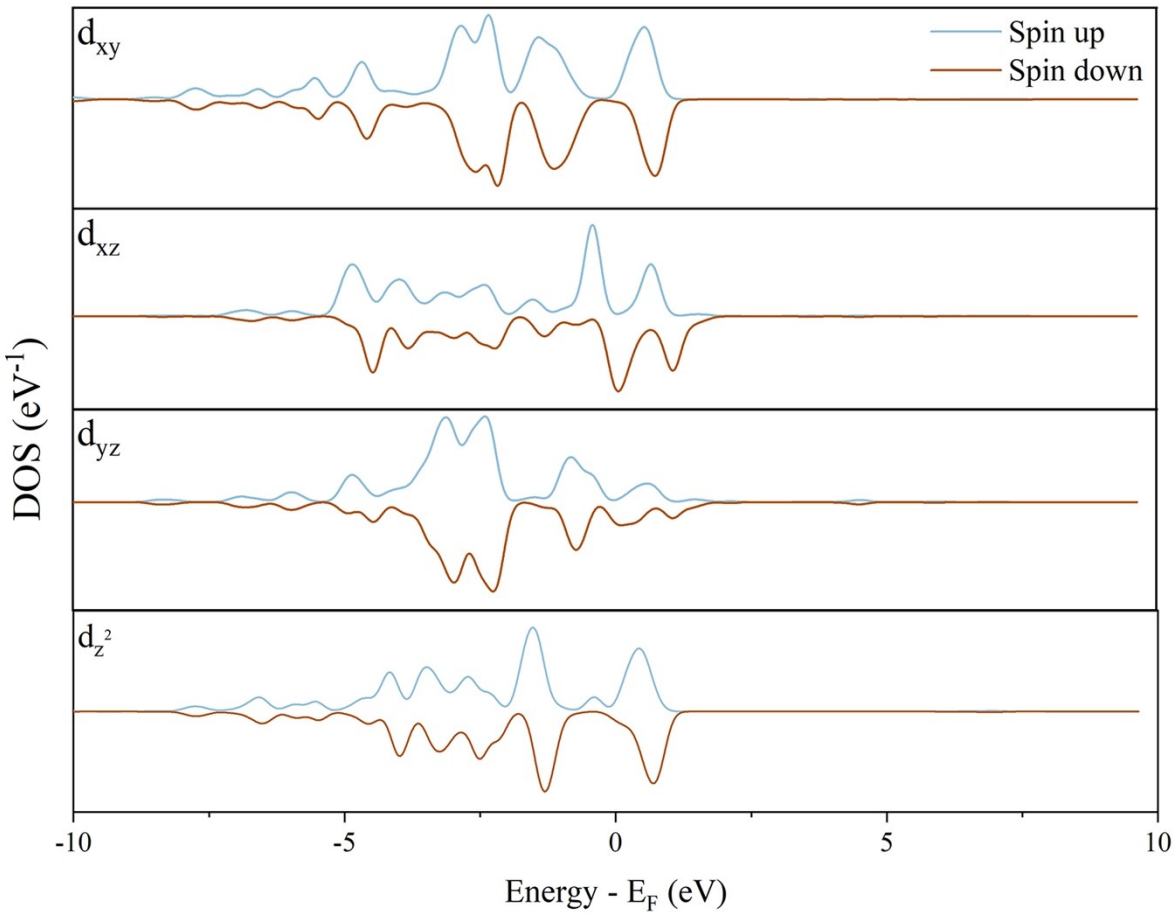

Figure S42. Contribution of different Ni 3d orbital directions on dxy, dxz, dyz, and dz^2 orbitals to the DOS of NiOOH-PmPz.

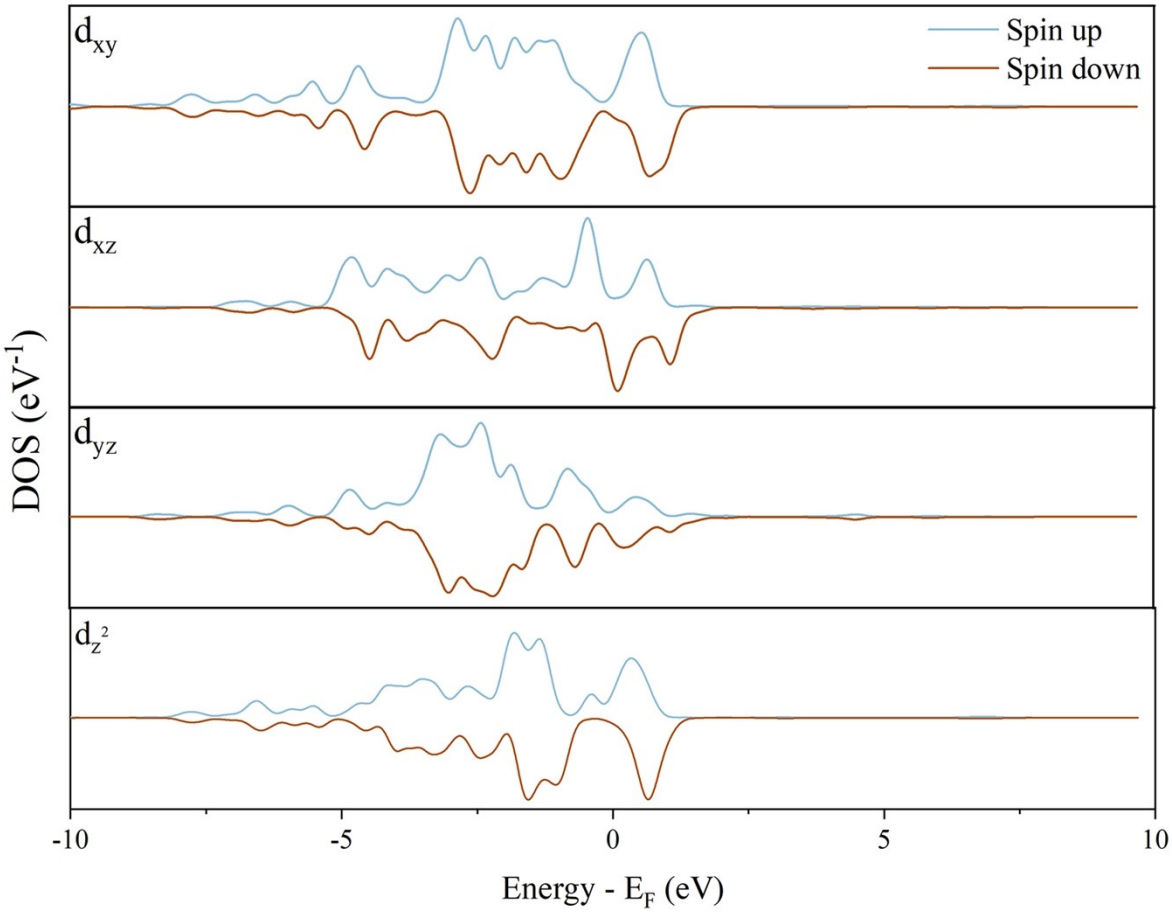

Figure S43. Contribution of different Ni 3d orbital directions on d_{xy}, d_{xz}, d_{yz}, and d_z^2 orbitals to the DOS of NiOOH-PmPz-Vo.

S3. Supporting Tables (Tables S1 – S5)

Table S1. Coordination number (*N*), amplitude reduction factor (S_0^2), energy shift (E_0), and calculated interatomic distances (*R*) of NiClOH-Pm and NiClOH-$Pm_{0.8}Pz_{0.2}$ before and after UOR.

	Atom pair	**N**	**S_0^2**	**E_0**	**R**
NiClOH-Pm	Ni-N	2	1.00	-1.453	2.058
	Ni-Cl	4	1.00	-1.453	2.397
NiClOH-Pm after UOR	Ni-O	6	0.83	-3.175	2.059
	Ni-Ni	6	0.83	-3.175	3.106
NiClOH-$Pm_{0.8}Pz_{0.2}$	Ni-N	2	1.00	-2.177	2.039
	Ni-Cl	4	1.00	-2.177	2.393
NiClOH-$Pm_{0.8}Pz_{0.2}$ after UOR	Ni-O	6	0.78	-3.491	2.061
	Ni-Ni	6	0.78	-3.491	3.109

Table S2. EDX spot analysis results (at%) of NiClOH-$Pm_{0.8}Pz_{0.2}$ before UOR.

C	N	O	Cl	Ni		SUM
25.61	20.73	3.10	27.40	23.16		100.00
24.54	17.20	2.07	29.50	26.69		100.00
24.76	16.82	1.66	30.37	26.39		100.00
22.73	15.97	1.55	31.37	28.37		100.00
28.99	17.15	2.32	26.42	25.12		100.00
27.58	18.36	2.64	26.59	24.83		100.00
AVERAGE						
25.70	17.71	2.22	28.61	25.76		

Table S3. EDX spot analysis results (at%) of NiClOH-$Pm_{0.8}Pz_{0.2}$ after UOR.

C	N	O	Cl	Ni		SUM
27.44	11.33	40.78	1.46	18.99		100.00
25.97	6.73	44.95	1.28	21.07		100.00
25.42	7.87	46.18	0.46	20.07		100.00
26.65	6.70	42.03	0.26	24.36		100.00
26.88	6.44	44.02	0.17	22.49		100.00
AVERAGE						
26.47	7.81	43.59	0.73	21.40		100.00

Table S4. ICP-MS (at%) results of NiClOH-$Pm_{0.8}Pz_{0.2}$ before and after electrochemical UOR tests.

	Cl (at%)	**Ni (at%)**
NiClOH-$Pm_{0.8}Pz_{0.2}$	31.95	27.75
NiClOH-$Pm_{0.8}Pz_{0.2}$ after UOR	11.40	26.25

Table S5. Electrocatalytic UOR performance of NiClOH-$Pm_{0.8}Pz_{0.2}$ compared with recently reported Ni-based catalysts.

Sample	Performance (vs. RHE)	Loading mass (mg cm^{-2})	Type of WE	Electrolyte	Ref.
E- LDH/α-FeOOH	1.32 V at 50 mA cm^{-2}	-	1 × 2 cm^2 NF	1 M KOH and 0.33 M Urea	9
Ni-SO_X	1.65 V at 323.4 mA cm^{-2}	~0.5	1 × 0.5 cm^2 CP	1 M KOH and 0.33 M Urea	10
$Ni_{1.6}Co_{0.4}P$/C	1.60 V at 140 mA cm^{-2}	0.5	0.0314 cm^2 GCE	1 M KOH and 0.33 M Urea	11
Li_xNiO_2	1.36 V at 5 mA cm^{-2}	-	1 × 1 cm^2 NF	1 M KOH and 0.50 M Urea	12
Pt–$Ni(OH)_2$@Ni-CNFs-2	1.363 V at 10 mA cm^{-2}	1	1 × 1 cm^2 CNF	1 M KOH and 0.33 M Urea	13
$NiWO_4$-TA950@Pt/C	1.49 V at 100 mA cm^{-2}	-	1 × 1 cm^2 NF	1 M KOH and 0.50 M Urea	14
$CoMn/CoMn_2O_4$@Co Mn/$CoMn_2O_4$	1.68 V at 100 mA cm^{-2}	-	1 × 1 cm^2 NF	1 M KOH and 0.50 M Urea	15
NiF_3/Ni_2P@CC-2	1.57 V at 100 mA cm^{-2}	~3.53	1 × 1.5 cm^2 CC	1 M KOH and 0.33 M Urea	16
Fe_3O_4@$NiCo_2O_4$/NiCo P	1.47 V at 50 mA cm^{-2}	-	2.5 × 3 cm^2 CC	1 M KOH and 0.50 M Urea	17
Rh-$LaNiO_3$	1.492 V at 10 mA cm^{-2}	1.5	1 × 1 cm^2 CP	1 M KOH and 0.33 M Urea	18
NiClOH-$Pm_{0.8}Pz_{0.2}$	1.37 V at 10 mA cm^{-2} 1.53 V at 100 mA cm^{-2} without iR correction	0.4	1 × 1 cm^2 CP	1 M KOH and 0.50 M Urea	this work

CP: carbon paper; NF: nickel foam; GCE: glassy carbon electrode; CC: carbon cloth

Table S6. Electrocatalytic biomass (methanol, ethanol, benzyl alcohol and glycerin) oxidation reaction performance of NiClOH-$Pm_{0.8}Pz_{0.2}$ compared with recently reported Ni-based catalysts.

Sample	Performance	Loading mass (mg cm^{-2})	Type of WE	Electrolyte	Ref.
Methanol					
O-vacant NiOOH	1.32 V (onset potential) 1.39 V at 1.0 mA cm^{-2}	-	ITO	1 M KOH, 0.5 M Methanol	19
NR–$Ni(OH)_2$	1.37 V (onset potential)	-	CC	1 M KOH, 0.5 M Methanol	20
Ni─MoN/NF-6	1.41 V (onset potential) 1.48 V at 100 mA cm^{-2}	-	1 × 1 cm^2 NF	1 M KOH, 0.5 M Methanol	21
Cr-doped α-$Ni(OH)_2$	1.302 V (onset potential) 1.424 V at 141 mA cm^{-2}	0.277	7.07 mm^2 GCE	1 M KOH, 0.5 M Methanol	22
$Cr_{0.02}$-$Ni(OH)_2$	1.34 V (onset potential) 1.45 V at 50 mA cm^{-2}	-	3 × 4 cm^2 NF	1 M KOH, 1 M Methanol	23
NiClOH-$Pm_{0.8}Pz_{0.2}$	1.35 V at 10 mA cm^{-2} 1.62 V at 100 mA cm^{-2} without iR correction	0.4	1 × 1 cm^2 CP	1 M KOH, 0.5 M Methanol	this Work
Ethanol					
B-Ni_2P/CoP/NF	1.38 V at 10 mA cm^{-2} 1.45 V at 50 mA cm^{-2}	-	1 × 1 cm^2	1 M KOH and 1 M Ethanol	24
Discrete $Ni(OH)_2$	1.40 V (onset potential) 1.78 V at 107.7 mA cm^{-2}	-	0.204 cm^2 (ECSA) FTO	1 M KOH and 1 M Ethanol	25
$Co(OH)_2$@$Ni(OH)_2$	1.30 V at 10 mA cm^{-2} 1.39 V at 100 mA cm^{-2}	-	FTO	1 M KOH and 1 M Ethanol	26
o-c-$CoSe_2$-Ni	1.31 V at 10 mA cm^{-2}	20	0.25 cm^{-2} CC	1 M KOH and 1 M Ethanol	27
VR-β-$Ni(OH)_2$	1.35 V (onset potential)	0.2	0.196 cm^2 GCE	1 M KOH and 50 mM Ethanol	28
NiClOH-$Pm_{0.8}Pz_{0.2}$	1.37 V at 10 mA cm^{-2} 1.57 V at 100 mA cm^{-2} without iR correction	0.4	1 × 1 cm^2 CP	1 M KOH, 0.5 M Ethanol	this work
Benzyl alcohol (BA)					
Ni_2P-O-300	1.33 V at 10 mA cm^{-2}	-	1 × 1 cm^2 NF	1 M KOH and 50 mM BA	29
PA-NF	1.31 V at 10 mA cm^{-2}	-	1 × 1 cm^2 NF	1 M KOH and 50 mM BA	30
FeCoNiAlMo/CNT	1.53 V at 100 mA cm^{-2}	5	CP	1 M KOH +	31

				0.2 M BA	
Ni–FeOOH thin films	1.35 V at 1 mA cm^{-2}	-	0.196 cm^2 Pt	1 M KOH and 50 mM BA	32
hp-Ni	~1.35 V (onset potential)	75	0.5 × 0.5 cm^2 NF	1 M KOH and 50 mM BA	33
NiClOH-$Pm_{0.8}Pz_{0.2}$	1.37 V at 10 mA cm^{-2} 1.75 V at 100 mA cm^{-2} without iR correction	0.4	1 × 1 cm^2 CP	1 M KOH, 0.5 M BA	this work
Glycerol					
Cu–NiCo/NF	1.23 V (10 mA cm^{-2}) 1.29 V (50 mA cm^{-2}) 1.33 V (100 mA cm^{-2})	-	1 × 1 cm^2 NF	1.0 M KOH and 0.1 M Glycerol	34
$Cu_xNi_{2-x}P$	1.41 (onset potential)	-	2 × 1 cm^2 NF	1 M KOH + 10 mM Glycerol	35
$Ni_{0.1}Co_{0.9}$@NiSACoSA-NCNTs	1.15 (onset potential)	-	2 × 3 cm^2 CC	1.0 M KOH and 0.1 M Glycerol	36
NiSex/Ni NRAs	1.31 V at 10 mA cm^{-2} 1.43 V at 50 mA cm^{-2} 1.52 V at 100 mA cm^{-2}	-	1 × 1 cm^2 Nickel foil	1.0 M KOH and 0.1 M Glycerol	37
CoNiCuMnMo-NPs/CC	1.25 V at 10 mA cm^{-2}	~1.1	1 × 1 cm^2 CC	1.0 M KOH and 0.1 M Glycerol	38
NiClOH-$Pm_{0.8}Pz_{0.2}$	1.47 V at 10 mA cm^{-2} 1.82 V at 100 mA cm^{-2} without iR correction	0.4	1 × 1 cm^2 CP	1 M KOH, 0.5 M Glycerol	this work

References

1. Chen, Z.; Li, J.; Meng, L.; Li, J.; Hao, Y.; Jiang, T.; Yang, X.; Li, Y.; Liu, Z. P.; Gong, M. Ligand vacancy channels in pillared inorganic-organic hybrids for electrocatalytic organic oxidation with enzyme-like activities. *Nat. Commun.* **2023**, *14* (1), 1184.

2. Ravel, B.; Newville, M.; Athena, A. Hephaestus: Data analysis for X-ray absorption spectroscopy using IFEFFIT, *J. Synchr. Radiat.* **2005,** 12, 537–541.

3. Ankudinov, A. L.; Ravel, B.; Rehr, J.; Conradson, S. Real-space multiple-scattering calculation and interpretation of X-ray-absorption near-edge structure. *Phys. Rev. B* **1998**, *58* (12), 7565.

4. Blöchl, P. E. Projector augmented-wave method. *Phys. Rev. B* **1994**, *50* (24), 17953.

5. Perdew, J. P.; Burke, K.; Ernzerhof, M. Generalized gradient approximation made simple. *Phys. Rev. Lett.* **1996**, *77* (18), 3865.

6. Anisimov, V. I.; Zaanen, J.; Andersen, O. K. Band theory and mott insulators: Hubbard U instead of stoner I. *Phys. Rev. B* **1991**, *44* (3), 943.

7. Cococcioni, M.; de Gironcoli, S. Linear response approach to the calculation of the effective interaction parameters in the LDA+U method. *Phys. Rev. B* **2005**, *71* (3), 035105.

8. Vanderbilt, D. Soft self-consistent pseudopotentials in a generalized eigenvalue formalism. *Phys. Rev. B* **1990**, *41* (11), 7892.

9. Cai, M.; Zhu, Q.; Wang, X.; Shao, Z.; Yao, L.; Zeng, H.; Wu, X.; Chen, J.; Huang, K.; Feng, S. Formation and stabilization of NiOOH by introducing α-FeOOH in LDH: Composite electrocatalyst for oxygen evolution and urea oxidation reactions. *Adv. Mater.* **2023**, *35* (7), 2209338.

10. Gao, X.; Bai, X.; Wang, P.; Jiao, Y.; Davey, K.; Zheng, Y.; Qiao, S.-Z. Boosting urea electrooxidation on oxyanion-engineered nickel sites via inhibited water oxidation. *Nat. Commun.* **2023**, *14* (1), 5842.

11. Rezaee, S.; Shahrokhian, S. 3d ternary $Ni_xCo_{2-x}P$/C nanoflower/nanourchin arrays grown on HCNs: A highly efficient bi-functional electrocatalyst for boosting hydrogen production via the urea electro-oxidation reaction. *Nanoscale* **2020**, *12* (30), 16123.

12. Han, W.-K.; Wei, J.-X.; Xiao, K.; Ouyang, T.; Peng, X.; Zhao, S.; Liu, Z.-Q. Activating lattice oxygen in layered lithium oxides through cation vacancies for enhanced urea electrolysis. *Angew. Chem. Int. Ed.* **2022**, *61* (31), e202206050.

13. Zhong, M.; Xu, M.; Ren, S.; Li, W.; Wang, C.; Gao, M.; Lu, X. Modulating the electronic structure of $Ni(OH)_2$ by coupling with low-content pt for boosting the urea oxidation reaction enables significantly promoted energy-saving hydrogen production. *Energy Environ. Sci.* **2024**, *17* (5), 1984.

14. Lin, R.; Kang, L.; Zhao, T.; Feng, J.; Celorrio, V.; Zhang, G.; Cibin, G.; Kucernak, A.; Brett, D. J. L.; Corà, F.; et al. Identification and manipulation of dynamic active site deficiency-induced competing reactions in electrocatalytic oxidation processes. *Energy Environ. Sci.* **2022**, *15* (6), 2386.

15. Wang, C.; Lu, H.; Mao, Z.; Yan, C.; Shen, G.; Wang, X. Bimetal schottky heterojunction boosting energy-saving hydrogen production from alkaline water via urea electrocatalysis. *Adv. Funct. Mater.* **2020**, *30* (21), 2000556.

16. Wang, K.; Huang, W.; Cao, Q.; Zhao, Y.; Sun, X.; Ding, R.; Lin, W.; Liu, E.; Gao, P. Engineering NiF_3/Ni_2P heterojunction as efficient electrocatalysts for urea oxidation and splitting. *Chem. Eng. J.* **2022**, *427*, 130865.

17. Sha, L.; Yin, J.; Ye, K.; Wang, G.; Zhu, K.; Cheng, K.; Yan, J.; Wang, G.; Cao, D. The construction of self-supported thorny leaf-like nickel-cobalt bimetal phosphides as efficient bifunctional electrocatalysts for urea electrolysis. *J. Mater. Chem. A* **2019**, *7* (15), 9078.

18. Kang, W.; Wu, S.; Li, Z.; Li, Z.; Li, K.; Wang, H. Highly stable urea oxidation electrolysis via Rh nanoparticles residing in the porous $LaNiO_3$ nanocubes. *Int. J. Hydrog. Energy* **2024**, *56*, 16.

19. Phan, V. T. T.; Nguyen, Q. P.; Wang, B.; Burgess, I. J. Oxygen vacancies alter methanol oxidation pathways on niooh. *J. Am. Chem. Soc.* **2024**, *146* (7), 4830.

20. Li, J.; Wu, C.; Wang, Z.; Meng, H.; Zhang, Q.; Tang, Y.; Zou, A.; Zhang, Y.; Zhong, H.; Xi, S.; et al. Unveiling the pivotal role of $d_{x^2-y^2}$ electronic states in nickel-based hydroxide electrocatalysts for methanol oxidation. *Angew. Chem. Int. Ed.* **2024**, *63* (25), e202404730.

21. Rao, C.; Wang, H.; Chen, K.; Chen, H.; Ci, S.; Xu, Q.; Wen, Z. Hybrid acid/base electrolytic cell for hydrogen generation and methanol conversion implemented by bifunctional Ni/MoN nanorod electrocatalyst. *Small* **2024**, *20* (7), 2303300.

22. Fan, Y.; Yang, X.; Wei, E.; Dong, Y.; Gao, H.; Luo, X.; Yang, W. Promoted electro-oxidation kinetics in chromium-

doped α-$Ni(OH)_2$ nanosheets for efficient selective conversion of methanol to formate. *Appl. Catal. B Environ*. **2024**, *345*, 123716.

23. Qin, H.; Ye, Y.; Lin, G.; Zhang, J.; Jia, W.; Xia, W.; Jiao, L. Regulating the electrochemical microenvironment of $Ni(OH)_2$ by Cr doping for highly efficient methanol electrooxidation. *ACS Catal.* **2024**, *14* (21), 16234.

24. Jia, L.; Wang, Y.; Duan, D.; Zhou, X.; Liu, S.; Wei, Q. B doped cobalt-nickel bimetallic phosphide as bifunctional catalyst for ethanol oxidation reaction and hydrogen evolution reaction. *J. Alloys Compd.* **2024**, *984*, 173974.

25. Zhang, Z.; Dong, Y.; Carlos, C.; Wang, X. Surface ligand modification on ultrathin $Ni(OH)_2$ nanosheets enabling enhanced alkaline ethanol oxidation kinetics. *ACS Nano* **2023**, *17* (17), 17180.

26. Li, Z.; Ning, S.; Xu, J.; Zhu, J.; Yuan, Z.; Wu, Y.; Chen, J.; Xie, F.; Jin, Y.; Wang, N.; et al. In situ electrochemical activation of $Co(OH)_2$@$Ni(OH)_2$ heterostructures for efficient ethanol electrooxidation reforming and innovative zinc–ethanol–air batteries. *Energy Environ. Sci.* **2022**, *15* (12), 5300.

27. Ye, Y.; Xu, J.; Li, X.; Jian, Y.; Xie, F.; Chen, J.; Jin, Y.; Yu, X.; Lee, M.-H.; Wang, N.; et al. Orbital occupancy modulation to optimize intermediate absorption for efficient electrocatalysts in water electrolysis and zinc–ethanol–air battery. *Adv. Mater.* **2024**, *36* (23), 2312618.

28. Chen, W.; Shi, J.; Wu, Y.; Jiang, Y.; Huang, Y.-C.; Zhou, W.; Liu, J.; Dong, C.-L.; Zou, Y.; Wang, S. Vacancy-induced catalytic mechanism for alcohol electrooxidation on nickel-based electrocatalyst. *Angew. Chem. Int. Ed.* **2024**, *63* (4), e202316449.

29. Chen, L.; Yu, C.; Song, X.; Dong, J.; Han, Y.; Huang, H.; Zhu, X.; Xie, Y.; Qiu, J. Microscopic-level insights into P-O-induced strong electronic coupling over nickel phosphide with efficient benzyl alcohol electrooxidation. *Small* **2024**, *20* (31), 2306410.

30. Xue, Q.; Xia, Z.; Gou, W.; Bu, J.; Li, J.; Xiao, H.; Qu, Y. Identification and origination of the O*-dominated β-NiOOH intermediates with high intrinsic activity for electrocatalytic alcohol oxidation. *ACS Catal.* **2023**, *13* (1), 400.

31. Wang, Y.; Ni, M.; Yan, W.; Zhu, C.; Jiang, D.; Yuan, Y.; Du, H. Supported high-entropy alloys for electrooxidation of benzyl alcohol assisted water electrolysis. *Adv. Funct. Mater.* **2024**, *34* (11), 2311611.

32. Wei, L.; Hossain, M. D.; Boyd, M. J.; Aviles-Acosta, J.; Kreider, M. E.; Nielander, A. C.; Stevens, M. B.; Jaramillo, T. F.; Bajdich, M.; Hahn, C. Insights into active sites and mechanisms of benzyl alcohol oxidation on nickel–iron oxyhydroxide electrodes. *ACS Catal.* **2023**, *13* (7), 4272.

33. You, B.; Liu, X.; Liu, X.; Sun, Y. Efficient H_2 evolution coupled with oxidative refining of alcohols via a hierarchically porous nickel bifunctional electrocatalyst. *ACS Catal.* **2017**, *7* (7), 4564.

34. Feng, Z.; Geng, Z.; Pan, S.; Yin, Y.; Sun, X.; Liu, X.; Ge, L.; Li, F. In situ patterning of nickel/sulfur-codoped laser-induced graphene electrode for selective electrocatalytic valorization of glycerol. *Appl. Catal. B Environ*. **2024**, *353*, 124101.

35. Ma, L.; Miao, Y.; Yang, J.; Fu, Y.; Yan, Y.; Zhang, Z.; Li, Z.; Shao, M. Promoting electrocatalytic glycerol C─C bond cleavage to formate coupled with H_2 production over a $Cu_xNi_{2-x}P$ catalyst. *Adv. Energy Mater.* **2024**, *14* (34), 2401061.

36. Zhang, Q.; Zhang, X.; Liu, B.; Jing, P.; Xu, X.; Hao, H.; Gao, R.; Zhang, J. Active hydroxyl-mediated preferential cleavage of carbon-carbon bonds in electrocatalytic glycerol oxidation. *Angew. Chem. Int. Ed.* **2025**, *64* (9), e202420942.

37. Wang, S.; Yan, Y.; Du, Y.; Zhao, Y.; Li, T.; Wang, D.; Schaaf, P.; Wang, X. Inhibiting the deep reconstruction of Ni-based interface by coordination of chalcogen anions for efficient and stable glycerol electrooxidation. *Adv. Funct. Mater.* **2024**, *34* (39), 2404290.

38. Fan, L.; Ji, Y.; Wang, G.; Chen, J.; Chen, K.; Liu, X.; Wen, Z. High entropy alloy electrocatalytic electrode toward alkaline glycerol valorization coupling with acidic hydrogen production. *J. Am. Chem. Soc.* **2022**, *144* (16), 7224.